RNA-Puzzles Round V: blind predictions of 23 RNA structures

Fan Bu, Yagoub Adam, Ryszard W Adamiak, Maciej Antczak, Belisa Rebeca H de Aquino, Nagendar Goud Badepally, Robert T Batey, Eugene F Baulin, Pawel Boinski, Michal J Boniecki, et al.

nature methods

Analysis

https://doi.org/10.1038/s41592-024-02543-9

RNA-Puzzles Round V: blind predictions of 23 RNA structures

Received: 15 February 2024

Accepted: 29 October 2024

Published online: 02 December 2024

Check for updates

A list of authors and their affiliations appears at the end of the paper

RNA-Puzzles is a collective endeavor dedicated to the advancement and improvement of RNA three-dimensional structure prediction. With agreement from structural biologists, RNA structures are predicted by modeling groups before publication of the experimental structures. We report a large-scale set of predictions by 18 groups for 23 RNA-Puzzles: 4 RNA elements, 2 Aptamers, 4 Viral elements, 5 Ribozymes and 8 Riboswitches. We describe automatic assessment protocols for comparisons between prediction and experiment. Our analyses reveal some critical steps to be overcome to achieve good accuracy in modeling RNA structures: identification of helix-forming pairs and of non-Watson–Crick modules, correct coaxial stacking between helices and avoidance of entanglements. Three of the top four modeling groups in this round also ranked among the top four in the CASP15 contest.

The prediction of RNA three-dimensional (3D) structure is challenging because of the complexity and variety of the noncovalent interactions involving the negatively charged phosphates, the stacking of the nucleobases and the hydrogen bonding between bases as well as between nucleotides. To address this challenge, the RNA-Puzzles project was established 12 years ago as a community-wide experiment to regularly evaluate the state of the art in RNA structure prediction[1–4]. The overall process is as follows. The organizers (E.W. or Z.M.) are contacted by a structural biologist who has solved and is about to publish an RNA-containing structure. The RNA sequence is confidentially distributed to the modeling groups that accepted to take part in the RNA-Puzzles contest. After taking into account the time span before publication of the data, a deadline is set for returning the predicted RNA models (generally 3–4 weeks for human-based predictions and 48 h for computer-only webserver predictions without human intervention). The name of the structural biologist group is not disclosed to the modeling groups. The process is thus double blind; the structure group is unknown to all and the structure is not present in any database. Each modeling group is entitled to use any technique or tool available to get insight on the RNA fold in human-based modeling. Later (see below), the modeling group has the opportunity to describe the tool and strategy used for the modeling. The project provides sequences, and occasionally additional data for a set of RNAs, and participants are challenged to predict their 3D structures before the experimentally determined structures are revealed. The RNA-Puzzles project promotes advances in the field of RNA structure prediction by stimulating the development of new algorithms and improvements of existing ones[1–4]. Furthermore, the RNA-Puzzles project includes continuous refinement of the assessment protocols. Depending on the resolution and the various functional states or experimental conditions of the experimentally determined structures, alternative RNA states, with local molecular details or large re-orientations of helices, can be observed. This renders fair and constructive comparisons between predicted and experimentally determined models difficult. The reporting process is as follows: first, automatic and specific comparisons between experimental and predicted models are described. Then, the modeling groups validate or comment on these assessments and describe the methods they used. Simultaneously, the structural biologists bring their own experimental expertise.

Results

Eighteen groups involved in 3D prediction of RNA participated in this round. See Methods for descriptions of the prediction tools used by each group. Each modeling group may submit sets of results obtained from multiple prediction approaches or protocols. Both automatic webserver predictions and predictions that include human-based input are received (within different deadlines) and analyzed separately. Of the 18 modeling approaches, only one is based on deep learning (Kollmann).

In the Supplementary Note, the sequences of all Puzzles can be found with, when applicable, a description of the sequence differences

e-mail: e.westhof@ibmc-cnrs.unistra.fr; miao_zhichao@gzlab.ac.cn

between the experimental and the modeled structures. The 23 Puzzles are classified into five functional groups: isolated RNA elements (four Puzzles), selected Aptamers bound to their specific ligand (two Puzzles), isolated Viral elements (four Puzzles), Ribozymes crystallized as the post-cleavage product (five Puzzles) and Riboswitches bound to their ligand (eight Puzzles). In RNA elements and Viral elements, comparisons between models and experimental structures focus on the RNA architectures. In the Aptamer and Riboswitch groups, beyond the RNA fold, the interest shifts to the RNA regions binding the ligand. In the present series of Puzzles, the RNAs are bound to their respective ligands; however, the riboswitches comprise three comparisons between experimental and modeled structures, PZ26, PZ27 and PZ28, where first the RNA T-box or tRNA ligand alone can be compared and, second, where the complexation between the RNAs is compared. This adds six further comparisons and leads to an overall number of 29 comparisons between experimental and modeled structures. For the successful predictions in the Ribozyme group, the catalytic residues are expected to be nearby. In short, the RNA element and Viral element categories allow the assessments of isolated RNAs, while the three other categories allow the assessments of the predictions of the RNA–Ligand interactions. The list of all Puzzles with short descriptions of the RNA molecule, the best-predicting group and the best root mean squared deviation (r.m.s.d.) reached, Protein Database (PDB) ID, resolution and references are summarized in Supplementary Table 1. RNA-Puzzles contests run on a rolling basis and, thus, the period spanning the various Puzzles is variable. Supplementary Table 1 gives the dates of the Puzzles (19 of 23 were carried out in the last 6 years).

In RNA-Puzzles[1–4], 3D RNA submissions are assessed within the context of the reference structure using the commonly used r.m.s.d.[5] and other RNA-specific scores, such as interaction network fidelity (INF)[6], deformation index (DI)[6] and an RNA-specific TM-score[7]. TM-score specific to RNA[7] is another global measure that can quantify the similarity of 3D RNA structures. Two further metrics were considered: the local Distance Difference Test (lDDT)[8] score and Atomic Rotationally Equivariant Scorer (ARES)[9]. The lDDT score emphasizes the local over the global accuracy. ARES is a score that should reflect the RNA-like nature of the folded RNAs. These various metrics were compared between each other. See Methods for full descriptions of the assessment metrics.

Prediction assessments

A superimposition between the experimental structure and the best-predicted model is shown for each Puzzle in Fig. 1 (the three comparisons between the tRNA ligands in Puzzles 26, 27 and 28 are not shown). Figure 1 shows that in several cases the overall fold is attained with the proper arrangement of helices with respect to each other; however, large deviations can be noticed for some Puzzles, especially in the Aptamers, Ribozymes or large Riboswitches, as analyzed below.

The distributions of the assessment metrics for the 29 comparisons between experimental structures and models are shown in Fig. 2. They display a large spread in assessment metrics, especially in r.m.s.d. and DI[6] (which reflects the spread in some INF[6] parameters). The spreads for the Clash score[10] and the INFall[6] are more limited with Clash scores <20 and the INFall >0.6 for most models. In the automatic web-based predictions (Supplementary Fig. 1) the spreads are less pronounced, but this could reflect the fact that the number of such predictions is much less than those that involve human expertise. The Spearman's correlation coefficients are poor between ARES[9] and r.m.s.d. or TM-score[7] but better between lDDT[8] (or INFall) and r.m.s.d. or TM-score. As noticed before[11], INFall and lDDT correlate well. The advantage of INFall[6] is that one can identify the contributions of its components (stacking, Watson–Crick pairs and non-Watson–Crick pairs).

The plots in Fig. 3 (top) show the distribution of the r.m.s.d. as a function of the RNA length (number of nucleotides) for experimental and model structures predicted with human expertise (Supplementary Fig. 2 for web-based predictions). The spread in r.m.s.d. has no clear dependence on length. In Fig. 3 (bottom), the scores reached by the various modeling groups (proportional to the number of times the models ranked first, second, etc., among the five best models) are given. Four groups stand out, three of which are the same as in the recent CASP15 (ref. 11) contest on a much smaller number of targets. For automatic webserver predictions, RNAComposer[12] (Szachniuk group) and SimRNA[13] (Bujnicki group) performed best with a slight preference for RNAComposer.

During the assembly of the RNA modular elements with junctions between them, it is difficult to avoid the formation of knots or entanglements. Supplementary Tables 2 and 3 present the number of entanglements and their types in the modeled structures calculated using RNAspider[14,15]. The most frequent case is a single strand going through an apical loop closing a helix (97 instances). In the Zika Viral element, the experimental structure shows the 3′-end about to form a knot. The highest number of entanglements was observed in PZ32, the Pepper aptamer.

The RNA elements

This group gathers four Puzzles (Supplementary Table 1): an RNA element from the 7SK RNA[16,17], two variants of the sarcin hairpin loop[18] and a fragment of the human telomerase RNA[19]. The two variants of the sarcin hairpin are mutations in the 26-mer r(UGCUCCUAGUACGAGAGGACCGGAGUG) that comprises nucleotides 2647-2673 in *Escherichia coli* 23S rRNA and was previously published[18]. The sarcin hairpin is characterized by a set of non-Watson–Crick. In PZ16a, the mutation is C2666A and, in PZ16b, the mutations are C2666A, U2653G and C2667A. Excellent agreements were generally obtained for these two Puzzles as can be seen in Supplementary Fig. 3 and Supplementary Fig. 4e–i. There is still a spread, surprising considering the structural homology, in the assessment metrics of the submitted models. Extended Data Fig. 1 displays some of the key non-Watson–Crick pairs. The triple interaction involving the *trans* W/H UA and the *cis* H/S UG is well reproduced in the best-modeled structure. However, the *trans* H/H AA pair is not reproduced correctly. The effect of the mutations at positions 2653 and 2667 is interesting: the contacts between the amino group of C2667 and the O2/O2′ of U2653 are reproduced by the amino group of A2667 with N3/O2′ of G2653. Although the G2653:A2667 is well reproduced in the modeling, the prediction of U2653:C2667 did not integrate that element of structural homology.

The other two Puzzles, PZ11 and PZ30, are difficult, especially PZ30, leading to the best r.m.s.d. around 5 Å. PZ11 contains several non-Watson–Crick pairs with protonated Cs or As, a possibility rarely considered in prediction programs. As can be seen from Supplementary Fig. 3a–d and Supplementary Fig. 4, the worst heat map regions in the DI involve these non-Watson–Crick pairs and bulges (for example A34, U40-U41, U63 and C75-A77). PZ30, a structure solved at a rather low resolution (3.80 Å) is a three-way junction with large unpaired segments linking the joining helices forming an open Y structure. It was solved as part of a larger complex (the human telomerase ribonucleoprotein) and interacts with a H2A–H2B histone dimer and the telomerase reverse transcriptase protein. Unsurprisingly, the largest deviations in the DI occur at single-stranded regions and apical loops.

The Aptamers

Two complexes between an aptamer and its fluorophore (Mango III[20] for PZ23 and Pepper[21] for PZ32) are in this group (Supplementary Table 1). PZ23 contains a double G-quartet on top of which stacks the fluorophore, as in related structures (Supplementary Fig. 5a–d). PZ32 does not contain a G-quartet but binds the fluorophore in a specific internal loop (Supplementary Fig. 5e–h). PZ23 represents a complex task due to its unusual structural features. Contrary to most RNA G4s, PZ23 exhibits a hybrid quadruplex containing two propeller loops and one lateral loop[22] (Extended Data Fig. 2a and Supplementary Fig. 5i). The *syn* conformations of G22 and G24, which form the two G-quartets, allow

https://doi.org/10.1038/s41592-024-02543-9

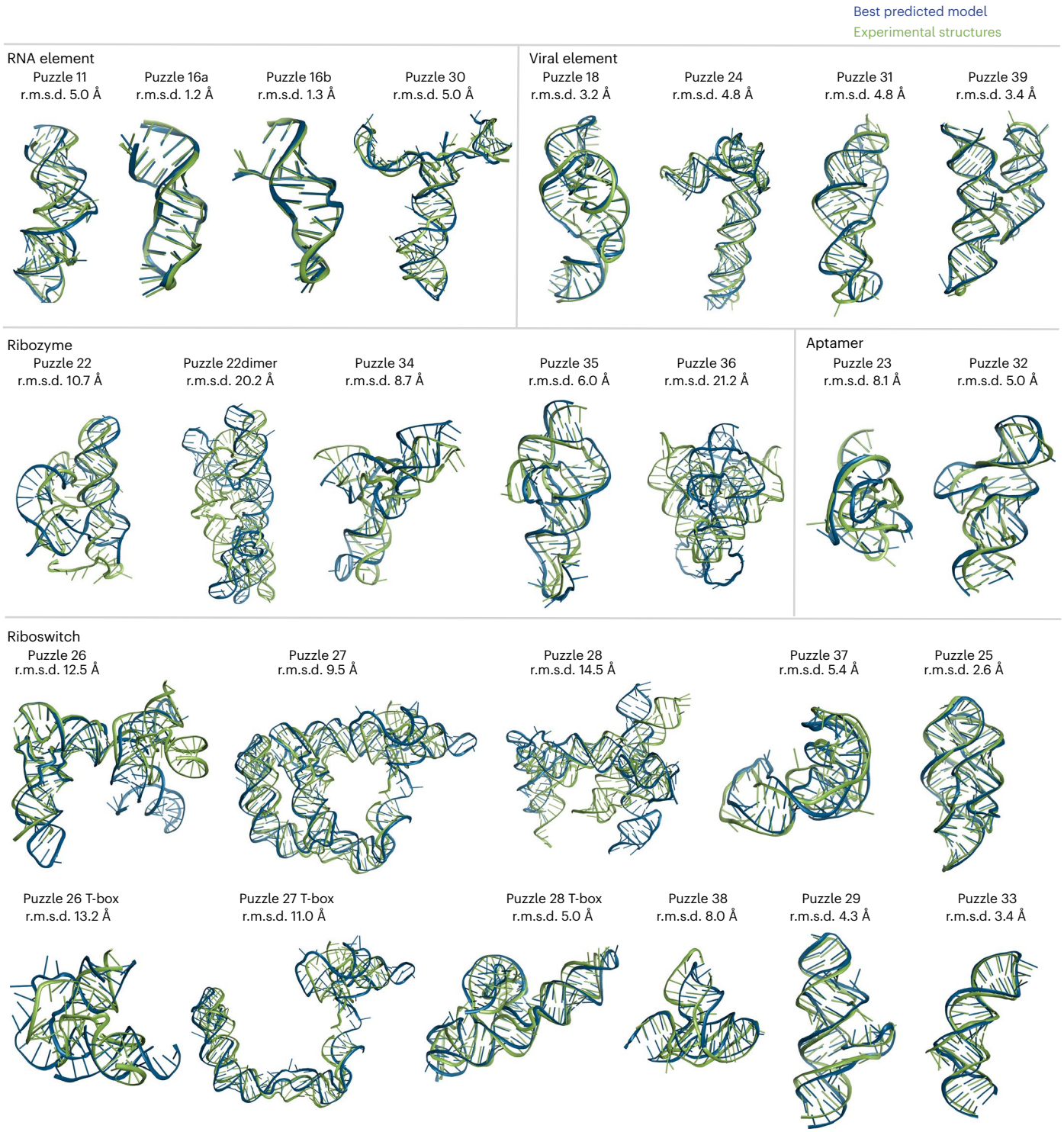

Fig. 1 | The best-predicted models superimposed on the experimental structures. Visualization of 26 targets (green) with the highest ranked model (blue) superimposed on each other (comparisons of the tRNAs in the T-box complexes are not shown). The selection of the best model was based on comparing the r.m.s.d. values of all five predicted models from all predictor groups to the available experimental structures. The best r.m.s.d. value is given beneath the corresponding Puzzle number. The five categories are: RNA element, Viral element, Aptamer, Ribozyme and Riboswitch. To simplify the visualization of RNA folding, the small molecule ligands are not displayed in this figure.

this arrangement (Supplementary Fig. 5i). All the groups assumed a typical parallel orientation with three propeller loops and all guanines in *anti*. This led to the selection of inappropriate guanosines for individual tetrads and, in effect, resulted in the improper fold of the quadruplex, as depicted in Extended Data Fig. 2b. This error propagated across residues 21–25 (Supplementary Fig. 5f). Only Bujnicki/SimRNA and Xiao models do not contain a quadruplex structure. In the case of PZ32, the overall fold is well reproduced, but the internal loops (6–10 and 29–32) display larger deviations in the DI (Supplementary Fig. 5f). Unexpectedly, rather large deviations are also seen at the UNCG apical tetraloop. For PZ23: seven groups made submissions (Bujnicki, Chen, Das, Ding, Dokholyan, Szachniuk and Xiao) with a fluorophore, but for PZ32,

https://doi.org/10.1038/s41592-024-02543-9

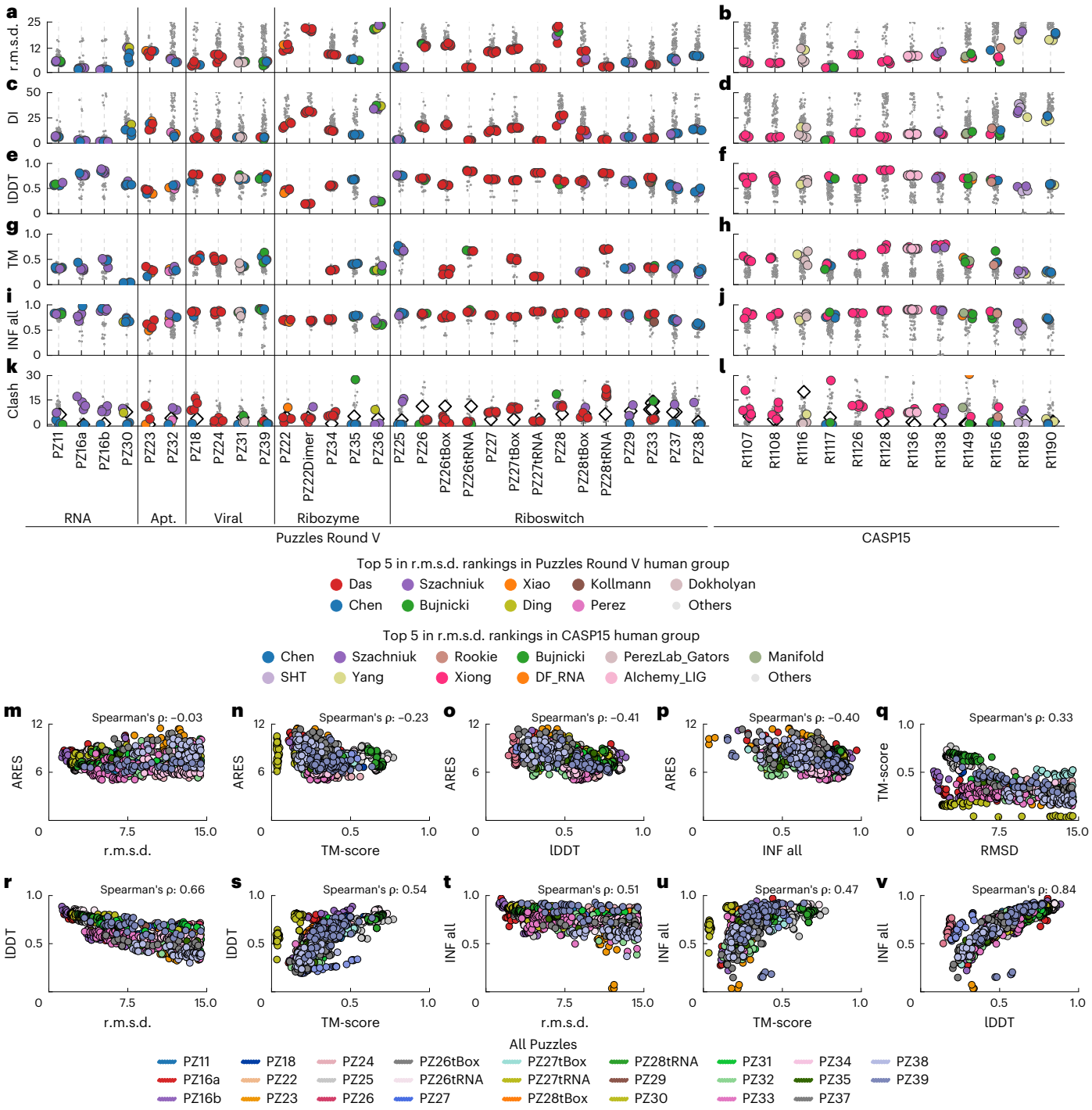

Fig. 2 | General analysis of the overall prediction results for all Puzzles with human expert predictions. a–**l**, The plots display the distribution of structure assessment metrics for all predicted groups for all Puzzles Round V. For comparison purposes, at the right are shown the data for the targets of CASP15 published previously. Each prediction model is represented by a dot, with each group having the same color. The assessment metrics include r.m.s.d. (Å) (**a**,**b**), DI (**c**,**d**), lDDT (**e**,**f**), TM-score (**g**,**h**), INF (**i**,**j**), where INFall includes all parameters (INFwc considers only the Watson–Crick pairs; INFnwc includes only the non-Watson–Crick pairs; and INFstack counts the stacked bases) and Clash score (**k**,**l**) where the black lozenge box indicates the solution structure. The legend below the plots indicates the best-performing group among all Puzzles. **m**–**v**, A correlation analysis between all models from Puzzles Round V across different metrics is presented. This analysis shows the interrelationships among the various evaluation metrics and helps to determine those that are positively correlated with the overall performance assessment of prediction models. Correlation plots between the metrics used for all Round V Puzzles with the Spearman's rank correlation coefficients (Spearman's ρ) indicated. ARES versus r.m.s.d. (Å) ($P = 0.37$) (**m**), ARES versus TM-score ($P = 0.00$) (**n**), ARES versus lDDT ($P = 0.00$) (**o**), ARES versus INFall ($P = 0.00$) (**p**), TM-score versus r.m.s.d. (Å) (P = 0.00) (**q**), lDDT versus r.m.s.d. (Å) ($P = 0.00$) (**r**), lDDT versus TM-score ($P = 0.00$) (**s**), INFall versus r.m.s.d. (Å) ($P = 0.00$) (**t**), INFall versus TM-score ($P = 0.00$) (**u**) and INFall versus lDDT ($P = 0.00$) (**v**). The r.m.s.d. was multiplied by −1 for calculating the correlations so that higher scores correspond to better accuracy for all metrics.

https://doi.org/10.1038/s41592-024-02543-9

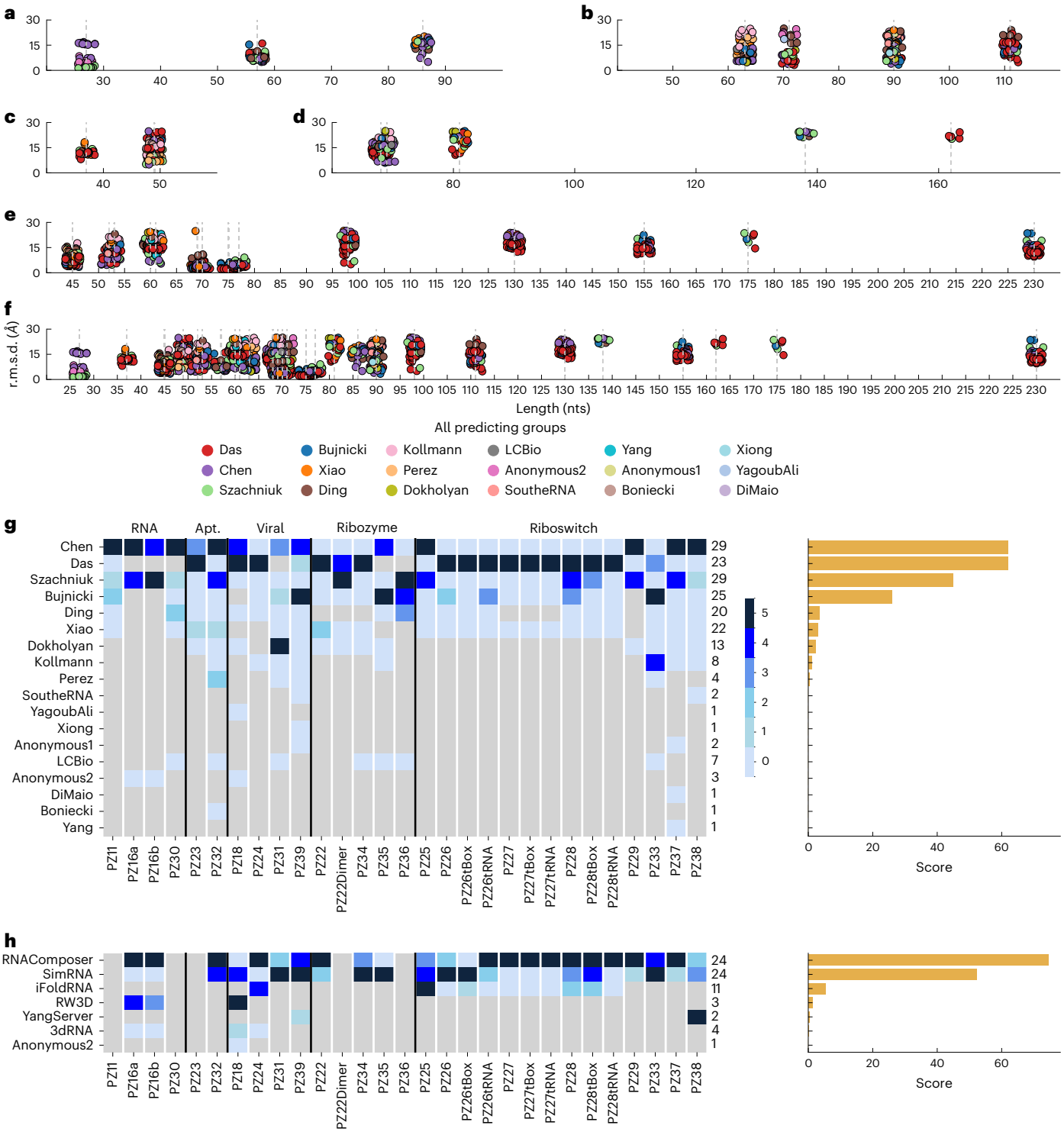

Fig. 3 | Correlation analysis between sequence length and r.m.s.d. for all Puzzles with human expert predictions. a–**e**, Scatter-plots are used to visualize the relations between r.m.s.d. and length within the prediction models classified into five groups: RNA element (**a**), Viral element (**b**), Aptamer (**c**), Ribozyme (**d**) and Riboswitch (**e**). **f**, All Puzzles are aggregated together. Each prediction model is depicted as a point on the scatter-plot. A similar plot for automatic webserver-based predictions is shown in Supplementary Fig. 2. **g**,**h**, Ranking of the modeling groups for human expert predictions (**g**) and for web-based predictions (**h**). For the left drawings of **g** and **h**, the color scheme (from dark to light blue) is such that 5 means that the group obtained the best r.m.s.d., 4 the second best and 1, the fifth best-predicted model, with 0 attributed when none of the submitted models was among the first five of the ranked models, when the group did not submit models for that Puzzle or the group was the only one to submit a model (shown in light gray). The last column of the right diagram is the total number of valid submissions to RNA-Puzzles (maximum 29) for each group. In the right drawings of **g** and **h**, the total sum reached by each group is given. The final score on the diagrams at the left of **g** and **h** is the total sum normalized by the ratio of valid submissions divided by the total number of Puzzles (29). The Das group submitted models coming from different methods and they are all gathered in a single group (Supplementary Table 5). The web-based predictions include RNAComposer (Szachniuk), SimRNA (Bujnicki), iFoldRNA (Dokholyan), RW3D (Das), YangServer (Yang) and 3dRNA (Xiao).

no prediction group submitted models with the fluorophore. Extended Data Fig. 2 shows the environments around the fluorophore in the experimental and in the best-predicted model (DAS_7, r.m.s.d. 8.1 Å). The sandwiching of the fluorophore between a G-quadruplex and U14 is predicted, despite the wrong choice of G24 within the quadruplex (instead of G22). Besides, U26 is contacting the fluorophore instead of U16. Fewer than half of the non-Watson–Crick pairs were correctly assigned in this complex fold.

The Viral elements

This group gathers four Puzzles, each from a different virus: Zika virus[23], adenovirus-associated RNA[24], SARS-CoV-2 (ref. 25) and the coxsackievirus B3 replication element[26] (Supplementary Table 1). The best r.m.s.d. reached are between 3.2 and 4.8 Å. Only the RNA element from the Zika virus, PZ18, had a homologous structure published before, and unsurprisingly, the best r.m.s.d. is the lowest, 3.2 Å; however, the spread of the r.m.s.d. distribution is important and extends from <5 Å to >25 Å. These Puzzles do not contain non-Watson–Crick pairs (except for PZ18) and the proper fold depends highly on the Watson–Crick pairs for which there is a large spread in the INFwc. Also, three Puzzles contain one pseudoknot (PZ18, PZ24 and PZ31) that was not always predicted. For PZ18, the DI map is clean and only two bulging nucleotides display deviations (U30 and A53) (Supplementary Fig. 6a–d). PZ24 is a complex RNA with two junctions separated by single-stranded regions, one three-way junction and a pseudoknot. The major deviations in the DI map occur in the apical loop of stem V and in the single-stranded regions of the three-way junction (Supplementary Fig. 6e–h). PZ31 is the programmed-1 ribosomal frameshifting RNA element of SARS-CoV-2. The sequence in the PDB (7mlx) is not exactly the one sent to the modeling groups (Supplementary Note). The modified nucleotides are not used in the comparisons. The discrepancies in the DI map occur at the ends of the three RNA helices and in single-stranded regions around S2. The region around the G13/G20 Hoogsteen/Watson–Crick in *trans* is shown in Extended Data Fig. 3a–f. Although residues 13, 20 and 21 are roughly in the same neighborhood, the non-Watson–Crick and stacking with U21 are not reproduced. It should be noted that independent structures of this element solved as a free RNA and on the mammalian ribosome by cryoelectron microscopy have a different global arrangement of the three helices[27,28] and a crystal structure of a slightly different sequence shows different details in non-Watson–Crick interactions[29].

PZ39 is an interesting four-way junction framed by C=G pairs with long-range non-Watson–Crick contacts between the apical loop L3 and a helical stack of three unusual pairs between pyrimidines (Supplementary Fig. 6m–p). The two coaxially stacked helical stems are parallel to each other without forming the pronounced X configuration in four-way junctions of RNA helices. A key long-range contact between L3 and the internal loop linking P4 and P4b locks in the four-way junction. The best r.m.s.d. reached is 3.4 Å with the inclusion of unpublished knowledge of the long-range contact and shows main deviations in the apical loops and in the internal loop between P4 and P4b. The contact between L3 and the internal loop consisting of three consecutive pyrimidine–pyrimidine pairs was well reproduced. The next best model has an r.m.s.d. of 4.0 Å, very close, with L3 folded and not pointing toward the internal loop P4/P4b. Notably, the best model submitted by an automatic webserver (from SimRNA, not shown) has an r.m.s.d. of 4.8 Å with the proper choice of coaxial stacks but without the long-range contact between L3 and the internal loop before P4. Figure 4 illustrates the large effects of wrong coaxial stacking choices on the r.m.s.d. Four-way junctions between blunt helices may adopt several arrangements of helices. Besides the choice of coaxial stackings (1–2 and 3–4 versus 1–4 and 2–3), the coaxial stacks can rotate about the crossing region leading to uncrossed and crossed helical arrangements. An illustrative comparison between human-based models shows that five out seven picked the correct coaxial stacking with crossed strands in two of them and the correct uncrossed choice in the best three models. The model with the largest r.m.s.d. does not have the proper coaxial stacking with the strands crossing at the central junction and an entanglement of two helical strands. From the table in Fig. 4, beyond an r.m.s.d. of around 11 Å, wrong choices in coaxial stacking and strand arrangements are very probable. Two groups also submitted webserver-based models for PZ39, SimRNA and RNAComposer. The same threshold was observed (not shown); <11 Å, the models had the correct arrangement of helices and, beyond that, wrong angles between helices or crossed strands as well as highly distorted models were observed.

The Ribozymes

Three different types of ribozymes, all products from the catalytic action, form this group: the nucleolytic hatchet ribozyme[30] (PZ22), the in vitro selected methyltransferase ribozyme[31] (PZ34) and the hepatitis delta virus (HDV)-like ribozyme, PZ35 for the human and PZ36 for the chimpanzee (CPEB3 HDV-like ribozyme)[32] (Supplementary Table 1). Two of them form dimers in the crystalline asymmetric unit, PZ22dimer and PZ36. PZ35 forms a dimer by crystallographic symmetry.

The hatchet ribozyme was predicted both as a monomer (PZ22) and a dimer (PZ22dimer). The formation of the PZ22 leads to complex intermolecular and intramolecular interactions and, unsurprisingly, the predictions for either the monomer or the dimer are difficult. We discuss one intramolecular contact (between L1 residues U7 to A11 and residues of the internal loop L3) (Extended Data Fig. 4f). The L1 loop is closed by a *trans* W/H U7/A11 pair as in T-like loops. U39 from L3 forms a *cis* W/S pair with G8. This specific contact locks in the relative orientation between L1 and the coaxial stack formed by P3 and P4. In Extended Data Fig. 4g, the same residues are represented and although they are in proximity, none of the exquisite contacts formed in the solution structure is present. There are three intermolecular helices formed between self-complementary segments in the 3′-end strands of L2/P2 of the monomers with the middle segment forming a single intermolecular helix and the segment ends forming two intermolecular helices (Extended Data Fig. 4a–c). In the best model, the central helix is formed, however, with a rotation of about 90° about the helical axis (Extended Data Fig. 4d,e), while the two other helices are not formed at all (Extended Data Fig. 4e), leading to large differences in the relative orientations of the monomers (Extended Data Fig. 4f,g).

PZ35 and PZ36 were already discussed in the joint assessment between CASP and RNA-Puzzles[11,32,33] where they had identifiers R1107 and R1108 (ref. 11). Here we will only discuss PZ36 where the chimpanzee CPEB3 HDV-like ribozyme forms an unexpected dimer in the crystal asymmetric unit (the same dimer is formed in the human HDV-like structure but with a crystallographic twofold axis). The single difference between the human and chimpanzee sequences is the A30G point mutation leading to the replacement of a Watson–Crick sugar-edge A–A base pair by a Watson–Crick G–C pair at the end of P1 in the chimpanzee ribozyme. Dimerization occurs by the formation of a four-stranded helix between palindromic self-complementary nucleotides of two antiparallel L3 loops (-ACGU-) (Extended Data Fig. 5a–b). In the best model structure, these two strands approach each other with a parallel orientation of the strands preventing the formation of base pairs (Extended Data Fig. 5c,d). The relative orientations of the two molecules in the dimer are therefore poorly predicted (Supplementary Fig. 7r). Those Puzzles were all very challenging and, again, the best r.m.s.d. (6.0 Å) was achieved for the HDV-like PZ35, as the structure of HDV was solved several years ago[32]. PZ34 is the methyltransferase ribozyme that transfers a methyl group between a G and AMP; it is a three-way junction with long single-stranded regions at the junction. The best-predicted model reached an r.m.s.d. of 8.7 Å with the largest deviations in the DI map in the UNCG tetraloop L2 of P2 and the 3′-end strand of P2 joining to P3 with large deviations for the relative orientations between L2 and P3. A single group (Dokholyan group) submitted a model with the ligand; unfortunately, that prediction is at an r.m.s.d. of 21.3 Å, a value too far away for meaningful comparisons.

https://doi.org/10.1038/s41592-024-02543-9

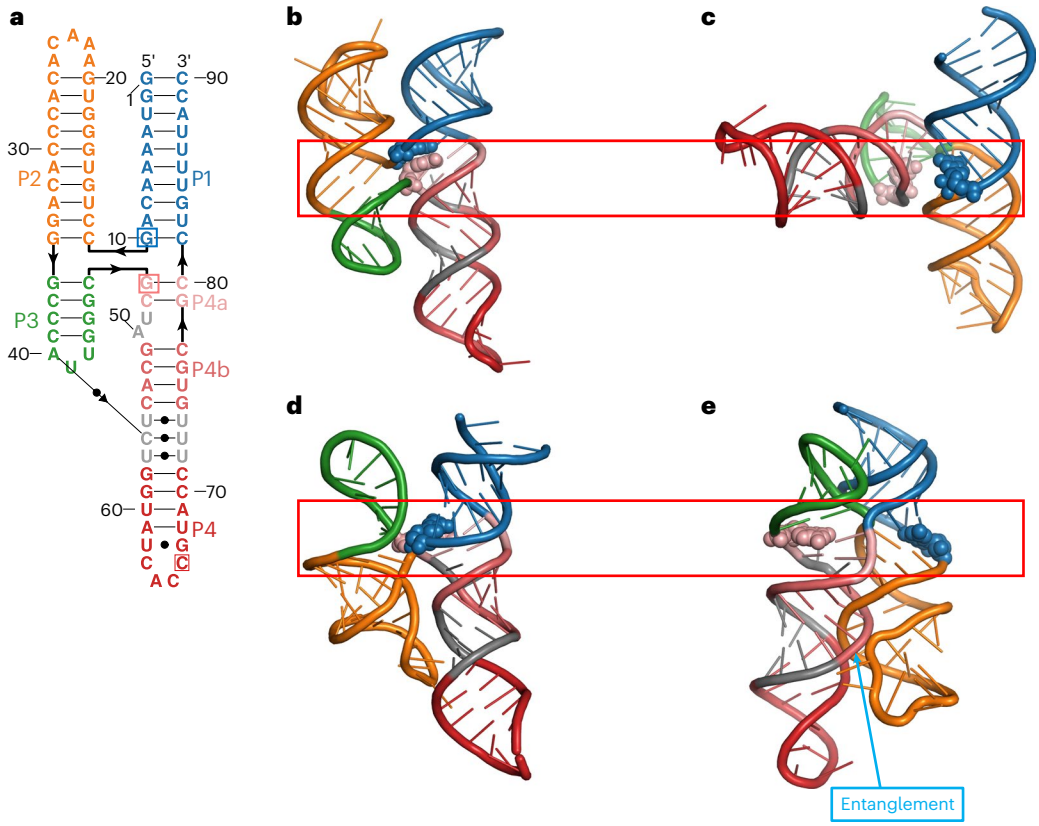

f

Name	Model	r.m.s.d.	INFall	TM-score	Stacking (G10–G47)	Label of structure
Chen	1	4.0	0.91	0.55	Yes + uncrossed	b
Ding	1	7.5	0.84	0.44	Yes + uncrossed	/
Szachniuk	2	10.9	0.87	0.46	Yes + uncrossed	/
Chen	10	16.4	0.86	0.26	No 90°	c
Dokholyan	1	20.0	0.85	0.30	Yes + crossed	d
Zhou	2	22.0	0.16	0.38	Yes + crossed	/
Xiao	1	24.0	0.78	0.28	No + crossed	e

Fig. 4 | Detailed analysis of PZ39, a four-way junction. a, Diagram of the secondary structure with the non-Watson–Crick pairs of the experimental structure (PDB ID: 8DP3) of Puzzle PZ39. In the experimental structure, P1 coaxially stacks with P4, and P2 with P3. The linking strands do not cross at the junction. The coaxial stacking is monitored by the stacking between G10 (blue square) and G47 (pink square), where the red rectangles indicate the critical coaxial regions. **b**–**e**, Predicted structures for PZ39. **f**, A table containing the modeling group with some metrics on the predicted model for the drawings represented in **b**–**e**, where 'Name' indicates the name of the prediction group and 'Model' indicates the number of the model submitted by the prediction group (ten models per group could be submitted for PZ39). Short descriptions about the stacking and arrangement of helices are also given. Note that in **e**, two strands intertwine and form an entanglement in which two closed loops intertwine.

In the Ribozyme category, the relative organization of the active site residues is key for understanding the catalytic mechanism. Functional and structural studies[34] have shown that, following catalysis, the active site residues stay close to each other in the nucleolytic and the methyltransferase[35] ribozymes. The predicted models were accordingly evaluated. In Extended Data Fig. 6, the core catalytic regions in PZ22 and PZ34 are compared by monitoring the distances between selected atoms of residues (Extended Data Fig. 6a,b) involved in catalysis[30,31]. In Extended Data Fig. 6c–f, the absolute values of the differences between these selected distances in the experimental and predicted structures are plotted as a function of the r.m.s.d. of the selected atoms (Extended Data Fig. 6c,d) or of the global r.m.s.d. (Extended Data Fig. 6e,f). For PZ22, three groups have low differences (less than 40 Å), Chen, Das and Szachniuk, and those three groups also reached the lowest r.m.s.d. For PZ34, two groups have models with the lowest distances (Das and Chen) with global r.m.s.d. around 9 Å. Extended Data Fig. 7 displays the predicted catalytic environments in the best models for PZ22 and PZ34. In the experimental structure (Extended Data Fig. 6a), A74 and A75 are splayed apart as well as G30 and G31. In none of the models is this pattern respected; they all show A74 and A75 stacked or in close proximity. For PZ34 (Extended Data Fig. 6b), the comparisons (Extended Data Fig. 7) show that, although the three key residues are in proximity, the orientations of the bases are far from optimal for catalysis.

The Riboswitches

This class gathers the largest number of Puzzles (eight), with three of them allowing multiple comparisons (the tRNA–Gly T-boxes) (Supplementary Figs. 8–10). All structures contain their bound ligands.

Three Puzzles, for which homologous structures or sequences were available, led to predictions <5 Å (PZ25, PZ29 and PZ33). The results for the T-box complexes are less satisfying (see below). PZ25 (ref. 36) is the best-modeled structure as it is the only one with

a homologous 3D structure. The ligand, 2′-deoxyguanosine (dG), binds to C51 and C78 (Extended Data Fig. 8). The ligand binding for the best-modeled structure is not perfect but it is very close in the second- and third-best-modeled structures (the base pair between the dG ligand and C62 is reproduced but not the contact between dG and C35). Of note, the third-ranked model is from the same group but web-based and the binding site region is not properly modeled. An additional point concerning PZ25 is that C43 is in the *syn* conformation in the crystal structure[36] (with short contact with O5′) and those best models all had C43 in the usual *anti* conformation. The *syn* conformation of C43 is likely the result of a modeling error during the structure determination. PZ29 is the NAD+ binding riboswitch[37]; it contains three regular helices interrupted by two asymmetric internal regions that form a two base-paired pseudoknot. The ligand binds in the minor groove of a C=G pair below an AA platform (Extended Data Fig. 8). The deviations in the DI map occur at the bulging A11 and the 3′-end strand of the pseudoknot. In contrast to the results obtained with PZ25, in none of the five highest best models is the ADP ligand close to the C6=G47, to which it binds via the sugar-edges in PZ29 (Extended Data Fig. 8).

The three Puzzles PZ26, PZ27 and PZ28 involve complexes between tRNA–Gly and part of or the complete T-box riboswitch (Supplementary Figs. 8 and 9). The outcomes of the predictions are mediocre, except for the T-box in PZ28. PZ26 is the complex between the tRNA bound to the T-box domain pairing to the -CCA end of the tRNA–Gly. The DI (Supplementary Fig. 9b) map shows clearly that stem III, which does not directly contact the tRNA, was observed to be located far away from where it was predicted to be. It should be noted that, in the experimental structure, nucleotide U131 is in the *syn* conformation and makes a *cis* H/W pair with C166. It is quite probable that U131 is in the *anti* conformation and forms a *cis* W/W with C166, as in most predicted models. PZ27 contains the domains of the T-box interacting with both the -CCA end and the anticodon loop of the tRNA. Surprisingly the T-box by itself was better predicted than the complex. The DI map of Supplementary Fig. 9j shows clearly that the tRNA is well predicted, except for the orientation of the T-loop (top right corner of the map) and, that in the T-box itself (bottom left corner), the regions not well positioned with respect to each other are in helices A1, A2 and stem III.

PZ33 is a riboswitch that binds xanthine[38]. Like PZ29, it is made of three regular helices interrupted by two asymmetric internal regions that form a single long-range Watson–Crick pair G35=C11 with G35 forming a sugar-edge/Watson–Crick pair with A39; xanthine binds to G10 and U40 located below those tertiary contacts. The best r.m.s.d. is 3.4 Å and the largest deviations in the DI map occur around those two critical regions, especially with respect to their relative orientations with P2b. The binding sites of the reacting ligands were not part of this Puzzle. PZ37 (ref. 39) and PZ38 (ref. 40) are two riboswitches binding NAD+ with PZ37 containing a single binding site and PZ38 containing two. It is a long hairpin with a large internal loop, the 5′-strand of which forms a pseudoknot with the single-stranded 3′-end that follows the hairpin. The common binding site is between two non-Watson–Crick pairs G41/C54 and U7/A55 (Supplementary Fig. 10o–s). The L1 loop was replaced by the U1A binding site in PZ37 and by AAAC in PZ38. Despite the sequence similarities, the prediction results differ. Figure 5 shows the different overall fold superimpositions and, in most cases, the lack of correct predictions for the non-Watson–Crick pairs (except in one case, Fig. 5b). PZ37 was modeled slightly better than PZ38, maybe because of the presence of the U1A loop and U1A protein. Most of the deviations are in the bulging residues (Supplementary Fig. 10n).

Discussion

We start with a discussion on several factors affecting the overall methodology. First, the RNA molecules must have a stable fold to form crystals or to be observed with cryo-EM technologies. For any ensemble of homologous RNA sequences, only a subset of them may have this property. Thus, we miss many aspects of the molecular dynamics of RNA molecules, either at the local (bulging or loop residues) or at the global level (alternative folds). On the other hand, analysis of such folded structures allows us to characterize the critical RNA elements participating in the construction and stability of the RNA fold common to homologous structures. Second, there is a contingent dependence on the availability of solved and unpublished structures. This is minimized to some extent in RNA-Puzzles by accepting new Puzzles on a rolling basis and then later gathering several Puzzles for publication. A possible drawback of this approach is that the methodologies used by the prediction groups evolve during the time span between Puzzle submission and publication. However, in the Methods the authors are careful to distinguish the various Puzzles and the methodologies they used. Third, the range in difficulty varies: there are Puzzles for which a homologous structure or a template can be found and others without any previously solved homologous structure. It is still valuable to assess structural models even when a published template is available. Besides, depending on the length of the single-strands connecting the helical elements, the prediction difficulty and the resulting accuracy can vary essentially because of the bulkiness of the right-handed RNA helices[11] coupled with the 5′ to 3′ polarity of the strands. Finally, the resolution of the experimental data is critical as it is generally related to the quality of the final experimental model (as evaluated for example by MolProbity[10]) and to the precision of the fit between the experimental model and the data.

We now consider RNA architecture, which is the global RNA fold and the key underlying local contacts. Here also, one can consider different levels of difficulty in the evaluation of accuracy. The first level, incorporated in the RNA-Puzzles assessment metrics, is the correct prediction of the Watson–Crick base pairs that form the helical scaffold. The resulting helices join at junctions of various complexity (two-way, three-way, four-way junctions, etc.) and the correct placement of helices at each of these junctions is necessary to reach some accuracy in the global fold. As discussed above, depending on the lengths of the single-stranded segments between helices, the number of choices for placing the helices varies considerably. In stably folded structures, one observes regularly that residues not involved in the formation of helices (within internal or apical loops) participate in the specific arrangement of the coaxial stacks of helices by forming non-Watson–Crick pairs, typical of the 3D architectures, which allow precise interaction contacts between long-range elements. Such non-Watson–Crick pairs, together with the stacking partners, constitute a second level of complexity. The recognition of such RNA–RNA interaction modules is key for reaching the observed 3D architecture. Here, several examples show that missing such architectural elements lead not only to local but especially global misfolded models. This was the case in PZ22 (Extended Data Fig. 4f,g). Many points involving analysis of the global fold and the local molecular contacts are valid for all categories of Puzzles. This is illustrated in Figs. 2 and 6 where the variations of most metrics do not depend much on the Puzzle categories (the better values come from homologous structures); however, the precise molecular contacts within the global fold (stacking and non-Watson–Crick pairs) are necessary to understand the specificity of ligand recognition and the roles of key residues for catalysis. A major conclusion is that good metrics in neither the secondary structure nor the global fold are sufficient to guarantee the correct identification of the residues involved in ligand recognition or catalysis.

The latter point is highlighted in the three categories, Aptamer, Ribozyme and Riboswitch, where the interest focuses on the residues contacting the ligand specifically or surrounding the active site. In the Aptamer category, Extended Data Fig. 2 shows a case where only a

https://doi.org/10.1038/s41592-024-02543-9

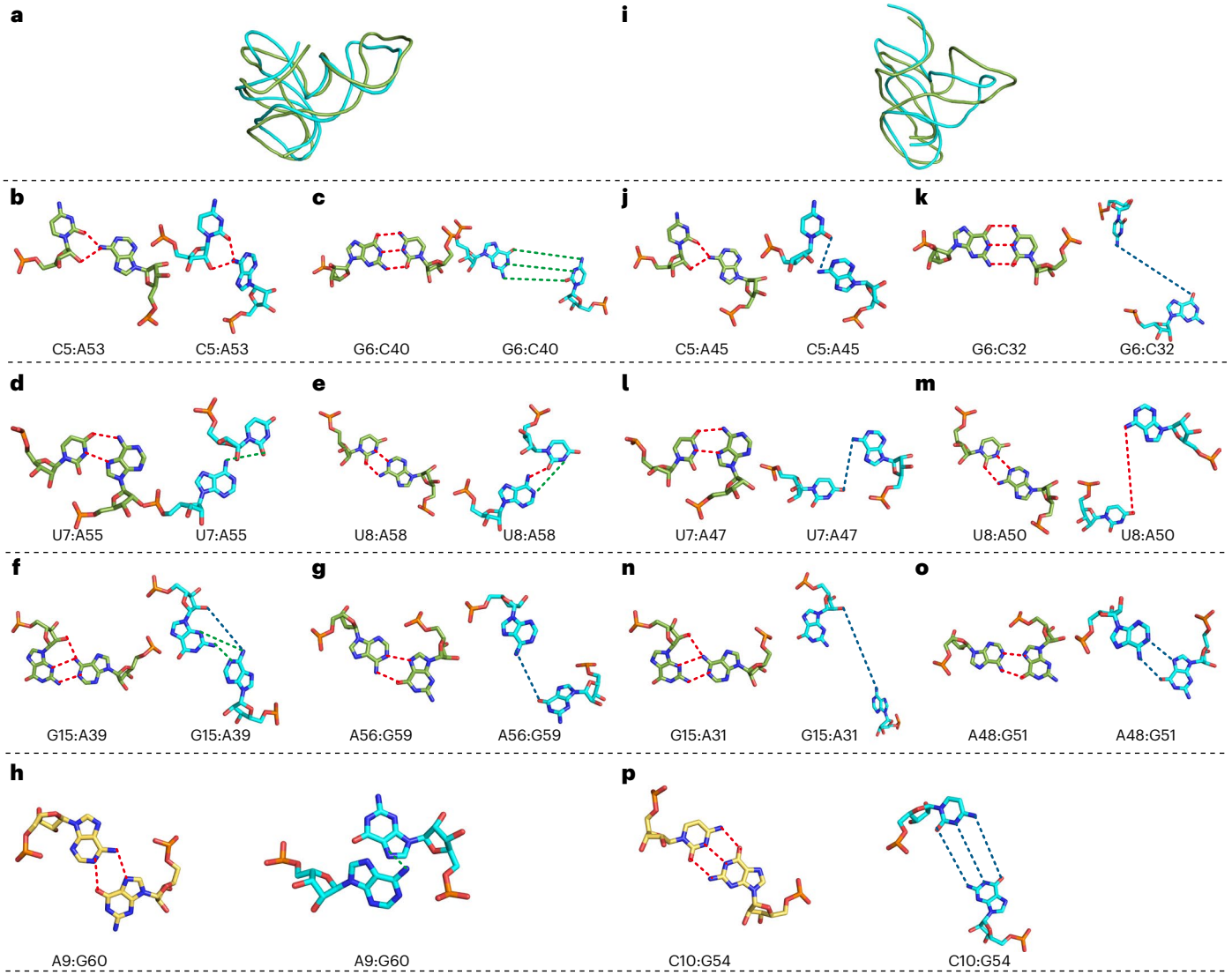

Fig. 5 | The detailed comparison analysis between experimental and best-predicted structures of the NAD+ II riboswitches PZ37/PZ38. **a**, Superimposition of the sugar-phosphate backbones of the experimental structure (resolution 2.5 Å) of PZ37 and of the best-predicted model (Chen_6, r.m.s.d. 5.4 Å). **b**–**g**, The drawings show specific base pair interactions in both experimental (with atomic bond distances in green) and predicted (with atomic bond distances in blue) structures. **i**, Superimposition of the sugar-phosphate backbones of the experimental structure (resolution 2.3 Å) of PZ38 and of the best-predicted model (Chen_3, r.m.s.d. 8.0 Å). **j**–**o**, The drawings show specific base pair interactions in both experimental (with atomic bond distances in green) and predicted (with atomic bond distances in blue) structures. The drawings of **h** and **p** represent unique base pair interactions found in PZ37 (**h**) or PZ38 (**p**). The experimental structures are shown with carbon atoms colored yellow and the predicted structures with carbon atoms colored cyan. The distances between atoms experimentally forming an H-bond are color-coded as a function of length <3.4 Å in red, 3.4–7 Å in green and >7 Å in dark blue.

fragment of the binding site was predicted. For ligand binding in the Riboswitch category, Fig. 5 and Extended Data Fig. 8 show that r.m.s.d. values between experimental and predicted models should be <2.7 Å (PZ25) to achieve meaningful results and that r.m.s.d. values >4.0 Å but still <5.0 Å (PZ29) do not lead to useful ligand-binding predictions. Because PZ25 is a purine riboswitch with available templates, more examples like these are needed to assess ligand-binding prediction accuracy. In the Ribozyme category, the relative organization and positions of the active site residues are not as close by as expected for understanding catalysis (Extended Data Fig. 7).

As discussed above, local contacts and global architecture are highly interconnected. Thus, the accuracy in the local contacts depends strongly on the achieved global fold as evaluated by standard r.m.s.d. Next, we compare r.m.s.d. values and their ranges. Some standard distances should be kept in mind: the distance between successive phosphate groups is of the order of 6–7 Å while the diameter of an RNA helix is 23 Å. r.m.s.d. values <5 Å imply a good accuracy. In the present paper, the analysis of PZ39 shows that >12 Å, some wrong choice in coaxial stacking is present, and >20 Å, the relative arrangement of helices (with potential formation of knots or helical entanglement) is incorrect compared to the experimental structure. In those cases, even strand mispairing and thus departure from secondary structure may be observed. Similar values relating r.m.s.d. values to architectures were reached following an analysis of PZ35 and PZ36 during CASP15 (ref. 41). It is recommended to check for the presence of such unusual strand interlockings using available tools[14].

We now consider precision of the modeled structures, as measured by the Clash score from MolProbity[10]. In the experimental structures considered here, only three had Clash scores >8 but <14 (PZ26, PZ29 and PZ33). Clash scores commonly observed experimentally at high resolution are below 5. Thus, one can consider three ranges, <5, 5–9 and >9. Values >15 indicate unusual atomic clashes or poor stereochemistry.

https://doi.org/10.1038/s41592-024-02543-9

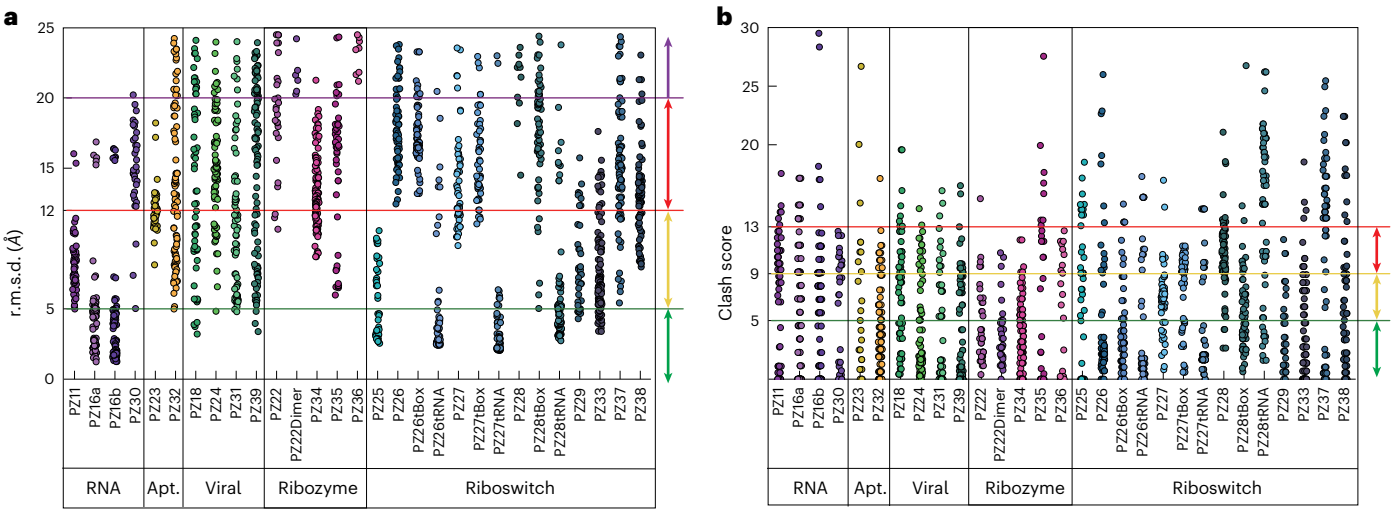

Fig. 6 | r.m.s.d. and Clash score for the 29 comparisons between experimental and all submitted predicted structures. a, For the r.m.s.d. plot, ranges delimited by analysis of the coaxial arrangement of helices are given. Below 4–5 Å, good accuracy can be achieved, but r.m.s.d. values <2.6–3.0 Å seem necessary for good ligand prediction. Between 4–5 and 11–12 Å, arrangements of helices can be correctly predicted; however, between 11–12 Å and 20 Å, wrong arrangements of helices are observed. Above 20 Å, wrong helical arrangements and even formation of entanglements or knots can be observed. **b**, Clash scores >10–15 are still commonly detected. Good experimental structures at high resolution have Clash scores between 3 and 5.

Although the Clash scores are in most cases <20, there are still models with much larger values in the present analysis, as well as in previous Puzzles[42]. Structures with high Clash scores tend also to contain entanglements[15]. Plots of the r.m.s.d. values and Clash scores of the 23 Puzzles with both human and webserver predictions are shown in Fig. 6 with the ranges discussed above marked. Good geometry and stereochemistry can be considered as a prerequisite for precision modeling, but they do not guarantee for accurate modeling as is exemplified in Supplementary Fig. 11.

Finally, we discuss the achievements of the modeling groups and comment on comparisons between human-based and automatic webserver predictions. Four groups were regularly present among the five best r.m.s.d. values (Bujnicki, Chen, Das and Szachniuk). Three of these groups (Bujnicki, Chen and Szachniuk) were also present in the top group of modelers in CASP15 (ref. 11) (the Das group participated in CASP15 as organizers and assessors, not as predictors).

These four modeling groups exploit the available database of RNA structures[43] to assemble and refine models under constraints based on specific force fields (Methods). VfoldRNA (Chen) integrates knowledge of RNA folds with a statistical model to calculate the free energy of folding and predict likely 3D formations. SimRNA (Bujnicki) uses coarse-grained (CG) molecular dynamics approaches to evaluate different conformations by scoring RNA interactions and identify stable, low-energy configurations. FARFAR2 (Das) refines initial fragment-based RNA assemblies by incorporating sophisticated sampling techniques and refined scoring functions for predicting RNA features and interactions. RNAcomposer (Szachniuk) uses a knowledge-based approach to assemble 3D structures guided by secondary structure constraints. These current methods encode certain RNA structure folding rules in various ways and allow for the intervention of human experts. Artificial intelligence tools, however, are powerful for abstracting and generalizing folding rules extracted from large datasets[44]. A combination of both approaches could be part of future directions in this field. Further, a strong advantage in RNA predictions is the frequent availability of many functionally homologous sequences that are expected to fold in similar architectures[45,46]. Thus, a systematic use of multiple sequence alignments would lead to more evolution-based modeling[47].

As in previous rounds of RNA-Puzzles, no single prediction method dominated Round V. The Chen and Das groups achieved a similar performance. For 14 of the 23 of the submitted comparisons, the best human-based model by r.m.s.d. came from Rosetta-based approaches by the Das group (Fig. 3g). Even within this set, a variety of 3D modeling approaches produced the model: one was from fragment assembly of RNA with full-atom refinement (FARFAR) with human selection, four from FARFAR2 with ARES selection and three from Stepwise Monte Carlo (SWM) with human selection. Given this variety of successful approaches, it is difficult to attribute better or worse performance to any particular 3D modeling method. Likely more important, as described in the Methods by the Das group, was the role of human expertise in inspecting the targets and previous literature, setting up appropriate modeling runs that might reflect information beyond just the target sequence and updating or developing new algorithms concomitantly with modeling. For all targets across all predictor groups, more automated workflows, such as RNAWorks3D or the ROSIE FARFAR2 server from the Das group, did not lead to better models than approaches where at least the setup of the modeling runs was informed by human expertise. In the automatic web-based predictions, RNAComposer (Szachniuk group) and SimRNA (Bujnicki group) performed well (Fig. 3h). While RNAComposer uses templates, SimRNA does not, and these different approaches might explain the slight difference in performance.

In Round IV, both human-based and automatic webserver predictions were available for only a small subset of Puzzles. In Extended Data Fig. 9, we show a similar analysis for Round IV (ref. 4) and the comparative values combining results on identical Puzzles from both Round IV and Round V. With this larger number of Puzzles, again both RNAComposer (Szachniuk group) and SimRNA (Bujnicki group) stand out (Extended Data Fig. 9b,d). As comparative analysis between automated methods and human expert groups is critical for evaluating current automated 3D structure prediction methods, RNA-Puzzles will continue to promote the systematic submission of both types of models.

Online content

Any methods, additional references, Nature Portfolio reporting summaries, source data, extended data, supplementary information, acknowledgements, peer review information; details of author contributions and competing interests; and statements of data and code availability are available at https://doi.org/10.1038/s41592-024-02543-9.

References

1. Cruz, J. A. et al. RNA-Puzzles: a CASP-like evaluation of RNA three-dimensional structure prediction. *RNA* **18**, 610–625 (2012).
2. Miao, Z. et al. RNA-Puzzles Round II: assessment of RNA structure prediction programs applied to three large RNA structures. *RNA* **21**, 1066–1084 (2015).
3. Miao, Z. et al. RNA-Puzzles Round III: 3D RNA structure prediction of five riboswitches and one ribozyme. *RNA* **23**, 655–672 (2017).
4. Miao, Z. et al. RNA-Puzzles Round IV: 3D structure predictions of four ribozymes and two aptamers. *RNA* **26**, 982–995 (2020).
5. Kabsch, W. A solution for the best rotation to relate two sets of vectors. *Acta Crystallogr. A* **32**, 922–923 (1976).
6. Parisien, M., Cruz, J. A., Westhof, E. & Major, F. New metrics for comparing and assessing discrepancies between RNA 3D structures and models. *RNA* **15**, 1875–1885 (2009).
7. Gong, S., Zhang, C. & Zhang, Y. RNA-align: quick and accurate alignment of RNA 3D structures based on size-independent TM-scoreRNA. *Bioinformatics* **35**, 4459–4461 (2019).
8. Mariani, V., Biasini, M., Barbato, A. & Schwede, T. lDDT: a local superposition-free score for comparing protein structures and models using distance difference tests. *Bioinformatics* **29**, 2722–2728 (2013).
9. Townshend, R. J. L. et al. Geometric deep learning of RNA structure. *Science* **373**, 1047–1051 (2021).
10. Williams, C. J. et al. MolProbity: More and better reference data for improved all-atom structure validation. *Protein Sci.* **27**, 293–315 (2018).
11. Das, R. et al. Assessment of three-dimensional RNA structure prediction in CASP15. *Proteins* **91**, 1747–1770 (2023).
12. Sarzynska, J., Popenda, M., Antczak, M. & Szachniuk, M. RNA tertiary structure prediction using RNAComposer in CASP15. *Proteins* **91**, 1790–1799 (2023).
13. Wirecki, T. K., Nithin, C., Mukherjee, S., Bujnicki, J. M. & Boniecki, M. J. Modeling of three-dimensional RNA structures using SimRNA. *Methods Mol. Biol.* **2165**, 103–125 (2020).
14. Luwanski, K. et al. RNAspider: a webserver to analyze entanglements in RNA 3D structures. *Nucleic Acids Res.* **50**, W663–W669 (2022).
15. Popenda, M. et al. Entanglements of structure elements revealed in RNA 3D models. *Nucleic Acids Res.* **49**, 9625–9632 (2021).
16. Martinez-Zapien, D. et al. The crystal structure of the 5′ functional domain of the transcription riboregulator 7SK. *Nucleic Acids Res.* **45**, 3568–3579 (2017).
17. Bourbigot, S. et al. Solution structure of the 5′-terminal hairpin of the 7SK small nuclear RNA. *RNA* **22**, 1844–1858 (2016).
18. Correll, C. C., Wool, I. G. & Munishkin, A. The two faces of the Escherichia coli 23S rRNA sarcin/ricin domain: the structure at 1.11 A resolution. *J. Mol. Biol.* **292**, 275–287 (1999).
19. Ghanim, G. E. et al. Structure of human telomerase holoenzyme with bound telomeric DNA. *Nature* **593**, 449–453 (2021).
20. Trachman, R. J. et al. Structure and functional reselection of the Mango-III fluorogenic RNA aptamer. *Nat. Chem. Biol.* **15**, 472–479 (2019).
21. Huang, K. et al. Structure-based investigation of fluorogenic Pepper aptamer. *Nat. Chem. Biol.* **17**, 1289–1295 (2021).
22. Adamczyk, B., Zurkowski, M., Szachniuk, M. & Zok, T. WebTetrado: a webserver to explore quadruplexes in nucleic acid 3D structures. *Nucleic Acids Res.* **51**, W607–W612 (2023).
23. Akiyama, B. M. et al. Zika virus produces noncoding RNAs using a multi-pseudoknot structure that confounds a cellular exonuclease. *Science* **354**, 1148–1152 (2016).
24. Hood, I. V. et al. Crystal structure of an adenovirus virus-associated RNA. *Nat. Commun.* **10**, 2871 (2019).
25. Roman, C., Lewicka, A., Koirala, D., Li, N.-S. & Piccirilli, J. A. The SARS-CoV-2 programmed −1 ribosomal frameshifting element crystal structure solved to 2.09 Å using chaperone-assisted RNA crystallography. *ACS Chem. Biol.* **16**, 1469–1481 (2021).
26. Das, N. K. et al. Crystal structure of a highly conserved enteroviral 5′ cloverleaf RNA replication element. *Nat. Commun.* **14**, 1955 (2023).
27. Zhang, K. et al. Cryo-EM and antisense targeting of the 28-kDa frameshift stimulation element from the SARS-CoV-2 RNA genome. *Nat. Struct. Mol. Biol.* **28**, 747–754 (2021).
28. Bhatt, P. R. et al. Structural basis of ribosomal frameshifting during translation of the SARS-CoV-2 RNA genome. *Science* **372**, 1306–1313 (2021).
29. Jones, C. P. & Ferré-D'Amaré, A. R. Crystal structure of the severe acute respiratory syndrome coronavirus 2 (SARS-CoV-2) frameshifting pseudoknot. *RNA* **28**, 239–249 (2022).
30. Zheng, L. et al. Hatchet ribozyme structure and implications for cleavage mechanism. *Proc. Natl Acad. Sci. USA* **116**, 10783–10791 (2019).
31. Deng, J. et al. Structure and mechanism of a methyltransferase ribozyme. *Nat. Chem. Biol.* **18**, 556–564 (2022).
32. Przytula-Mally, A. I. et al. Anticodon-like loop-mediated dimerization in the crystal structures of HDV-like CPEB3 ribozymes. Preprint at *bioRxiv* https://doi.org/10.1101/2022.09.22.508989 (2023).
33. Mulvaney, T. et al. CASP15 cryo-EM protein and RNA targets: Refinement and analysis using experimental maps. *Proteins* **91**, 1935–1951 (2023).
34. Deng, J. et al. Ribocentre: a database of ribozymes. *Nucleic Acids Res.* **51**, D262–D268 (2023).
35. McCarthy, E. et al. Catalytic mechanism and pH dependence of a methyltransferase ribozyme (MTR1) from computational enzymology. *Nucleic Acids Res.* **51**, 4508–4518 (2023).
36. Matyjasik, M. M. & Batey, R. T. Structural basis for 2′-deoxyguanosine recognition by the 2′-dG-II class of riboswitches. *Nucleic Acids Res.* **47**, 10931–10941 (2019).
37. Huang, L., Wang, J. & Lilley, D. M. J. Structure and ligand binding of the ADP-binding domain of the NAD riboswitch. *RNA* **26**, 878–887 (2020).
38. Xu, X. et al. Insights into xanthine riboswitch structure and metal ion-mediated ligand recognition. *Nucleic Acids Res.* **49**, 7139–7153 (2021).
39. Xu, X. et al. Structure-based investigations of the NAD+-II riboswitch. *Nucleic Acids Res.* **51**, 54–67 (2023).
40. Peng, X., Liao, W., Lin, X., Lilley, D. M. J. & Huang, L. Crystal structures of the NAD+-II riboswitch reveal two distinct ligand-binding pockets. *Nucleic Acids Res.* **51**, 2904–2914 (2023).
41. Kretsch, R. C. et al. RNA target highlights in CASP15: Evaluation of predicted models by structure providers. *Proteins* **91**, 1600–1615 (2023).
42. Carrascoza, F., Antczak, M., Miao, Z., Westhof, E. & Szachniuk, M. Evaluation of the stereochemical quality of predicted RNA 3D models in the RNA-Puzzles submissions. *RNA* **28**, 250–262 (2022).
43. Burley, S. K. et al. RCSB Protein Data Bank (RCSB.org): delivery of experimentally-determined PDB structures alongside one million computed structure models of proteins from artificial intelligence/machine learning. *Nucleic Acids Res.* **51**, D488–D508 (2022).
44. Varadi, M. et al. AlphaFold Protein Structure Database in 2024: providing structure coverage for over 214 million protein sequences. *Nucleic Acids Res.* **52**, D368–D375 (2024).
45. Kalvari, I. et al. RFAM 14: expanded coverage of metagenomic, viral and microRNA families. *Nucleic Acids Res.* **49**, D192–D200 (2021).

46. The RNAcentral Consortium, et al. RNAcentral: a hub of information for non-coding RNA sequences. *Nucleic Acids Res.* **47**, D1250–D1251 (2018).
47. Michel, F. & Westhof, E. Modelling of the three-dimensional architecture of group I catalytic introns based on comparative sequence analysis. *J. Mol. Biol.* **216**, 585–610 (1990).

Fan Bu[1,2], Yagoub Adam[3,4], Ryszard W. Adamiak[5,6], Maciej Antczak[5,6], Belisa Rebeca H. de Aquino[7], Nagendar Goud Badepally[7], Robert T. Batey[8], Eugene F. Baulin[7], Pawel Boinski[6], Michal J. Boniecki[7], Janusz M. Bujnicki[7], Kristy A. Carpenter[9], Jose Chacon[10,11], Shi-Jie Chen[12], Wah Chiu[13], Pablo Cordero[10,14], Naba Krishna Das[15], Rhiju Das[10,16,17], Wayne K. Dawson[7], Frank DiMaio[18,19], Feng Ding[20], Anne-Catherine Dock-Bregeon[21], Nikolay V. Dokholyan[22], Ron O. Dror[23,24,25,26], Stanisław Dunin-Horkawicz[7], Stephan Eismann[27,28], Eric Ennifar[29], Reza Esmaeeli[30], Masoud Amiri Farsani[7], Adrian R. Ferré-D'Amaré[31], Caleb Geniesse[10,32], George E. Ghanim[33], Horacio V. Guzman[34], Iris V. Hood[35], Lin Huang[36], Dharm Skandh Jain[7], Farhang Jaryani[7], Lei Jin[12], Astha Joshi[7], Masha Karelina[17,23], Jeffrey S. Kieft[37,38], Wipapat Kladwang[10,16], Sebastian Kmiecik[39], Deepak Koirala[15], Markus Kollmann[40], Rachael C. Kretsch[17], Mateusz Kurciński[39], Jun Li[12], Shuang Li[35], Marcin Magnus[7,41], BenoÎt Masquida[42], S. Naeim Moafinejad[7], Arup Mondal[30], Sunandan Mukherjee[7], Thi Hoang Duong Nguyen[33], Grigory Nikolaev[7], Chandran Nithin[7,39], Grace Nye[16], Iswarya P. N. Pandaranadar Jeyeram[7], Alberto Perez[30], Phillip Pham[16], Joseph A. Piccirilli[43,44], Smita Priyadarshini Pilla[45], Radosław Pluta[7], Simón Poblete[46,47], Almudena Ponce-Salvatierra[7], Mariusz Popenda[5], Lukasz Popenda[48], Fabrizio Pucci[49], Ramya Rangan[17,28], Angana Ray[7], Aiming Ren[50], Joanna Sarzynska[5], Congzhou Mike Sha[22], Filip Stefaniak[7], Zhaoming Su[51], Krishna C. Suddala[35], Marta Szachniuk[5,6], Raphael Townshend[23,28], Robert J. Trachman III[31], Jian Wang[22], Wenkai Wang[52], Andrew Watkins[10,53], Tomasz K. Wirecki[7], Yi Xiao[54], Peng Xiong[2,55], Yiduo Xiong[54], Jianyi Yang[52], Joseph David Yesselman[16,56], Jinwei Zhang[35], Yi Zhang[54], Zhenzhen Zhang[20], Yuanzhe Zhou[12], Tomasz Zok[6], Dong Zhang[12], Sicheng Zhang[12], Adriana Żyła[7], Eric Westhof[29,57] ✉ & Zhichao Miao[1,58,59] ✉

[1]GMU-GIBH Joint School of Life Sciences, The Guangdong-Hong Kong-Macao Joint Laboratory for Cell Fate Regulation and Diseases, Guangzhou National Laboratory, Guangzhou Medical University, Guangzhou, China. [2]School of Life Sciences, Division of Life Sciences and Medicine, University of Science and Technology of China, Hefei, China. [3]Inter-institutional Graduate Program on Bioinformatics, Department of Computer Science and Mathematics, FFCLRP, University of São Paulo, Ribeirão Preto, Brazil. [4]Covenant University Bioinformatics Research (CUBRe), Covenant University, Ota, Nigeria. [5]Institute of Bioorganic Chemistry, Polish Academy of Sciences, Poznan, Poland. [6]Institute of Computing Science, Poznan University of Technology, Poznan, Poland. [7]Laboratory of Bioinformatics and Protein Engineering, International Institute of Molecular and Cell Biology in Warsaw, Warsaw, Poland. [8]Department of Biochemistry, University of Colorado at Boulder, Boulder, CO, USA. [9]Department of Biomedical Data Science, Stanford University, Stanford, CA, USA. [10]Department of Biochemistry, Stanford University, Stanford, CA, USA. [11]Department of Cell and Developmental Biology, University of California San Diego, San Diego, CA, USA. [12]Department of Physics, Department of Biochemistry and Institute for Data Science and Informatics, University of Missouri, Columbia, MO, USA. [13]Department of Bioengineering and James H. Clark Center, Stanford University, Stanford, CA, USA. [14]Stripe, South San Francisco, CA, USA. [15]Department of Chemistry and Biochemistry, University of Maryland Baltimore County, Baltimore, MD, USA. [16]Howard Hughes Medical Institute, Stanford University, Stanford, CA, USA. [17]Biophysics program, Stanford University, Stanford, CA, USA. [18]Department of Biochemistry, University of Washington, Seattle, WA, USA. [19]Institute for Protein Design, University of Washington, Seattle, WA, USA. [20]Department of Physics and Astronomy, Clemson University, Clemson, SC, USA. [21]Laboratory of Integrative Biology of Marine Models (LBI2M), Sorbonne University-CNRS UMR8227, Roscoff, France. [22]Department of Pharmacology, Penn State College of Medicine, Hershey, PA, USA. [23]Department of Computer Science, Stanford University, Stanford, CA, USA. [24]Department of Structural Biology, Stanford University, Stanford, CA, USA. [25]Department of Molecular and Cellular Physiology, Stanford University, Stanford, CA, USA. [26]Institute for Computational and Mathematical Engineering, Stanford University, Stanford, CA, USA. [27]Department of Applied Physics, Stanford University, Stanford, CA, USA. [28]Atomic AI, South San Francisco, CA, USA. [29]Architecture et Réactivité de l'ARN, Institut de Biologie Moléculaire et Cellulaire du CNRS, Université de Strasbourg, Strasbourg, France. [30]Department of Chemistry and Quantum Theory Project, University of Florida, Gainesville, FL, USA. [31]Laboratory of Nucleic Acids, National Heart, Lung and Blood Institute, Bethesda, MD, USA. [32]Lawrence Berkeley National Laboratory, Berkeley, CA, USA. [33]Medical Research Council Laboratory of Molecular Biology, Cambridge, UK. [34]Instituto de Ciencia de Materials de Barcelona, ICMAB-CSIC, Bellaterra E-08193, Spain & Departamento de Física Teórica de la Materia Condensada, Universidad Autónoma de Madrid, Madrid, Spain. [35]Laboratory of Molecular Biology, National Institute of Diabetes and Digestive and Kidney Diseases, Bethesda, MD, USA. [36]Guangdong Provincial Key Laboratory of Malignant Tumor Epigenetics and Gene Regulation, Guangdong-Hong Kong Joint Laboratory for RNA Medicine, Sun Yat-Sen Memorial Hospital, Sun Yat-Sen University Guangzhou, Guangdong, China. [37]Department of Biochemistry and Molecular

Genetics, University of Colorado Denver School of Medicine, Aurora, CO, USA. [38]New York Structural Biology Center, New York, NY, USA. [39]Laboratory of Computational Biology, Biological and Chemical Research Center, Faculty of Chemistry, University of Warsaw, Warsaw, Poland. [40]Department of Computer Science, Heinrich Heine University of Düsseldorf, Düsseldorf, Germany. [41]Department of Molecular and Cellular Biology, Harvard University, Cambridge, MA, USA. [42]UMR 7156, CNRS - Université de Strasbourg, IPCB, Strasbourg, France. [43]Department of Biochemistry and Molecular Biology, The University of Chicago, Chicago, IL, USA. [44]Department of Chemistry, The University of Chicago, Chicago, IL, USA. [45]Laboratory of Computational Biology, Biological and Chemical Research Center, University of Warsaw, Warsaw, Poland. [46]Facultad de Ingeniería, Arquitectura y Diseño, Universidad San Sebastián, Santiago, Chile. [47]Centro BASAL Ciencia & Vida, Universidad San Sebastián, Santiago, Chile. [48]NanoBioMedical Centre, Adam Mickiewicz University, Poznan, Poland. [49]Computational Biology and Bioinformatics, Université Libre de Bruxelles, Brussels, Belgium. [50]Life Sciences Institute, Zhejiang University, Hangzhou, China. [51]The State Key Laboratory of Biotherapy, West China Hospital, Chengdu, China. [52]MOE Frontiers Science Center for Nonlinear Expectations, Research Center for Mathematics and Interdisciplinary Sciences, Shandong University, Qingdao, China. [53]Prescient Design, Genentech Research and Early Development, South San Francisco, CA, USA. [54]School of Physics and Key Laboratory of Molecular Biophysics of the Ministry of Education, Huazhong University of Science and Technology, Wuhan, China. [55]Department of Biomedical Engineering, Suzhou Institute for Advanced Research, University of Science and Technology of China, Suzhou, China. [56]Department of Chemistry, University of Nebraska, Lincoln, NE, USA. [57]Engineering Research Center of Clinical Functional Materials and Diagnosis & Treatment Devices of Zhejiang Province, Wenzhou Institute, University of Chinese Academy of Sciences, Wenzhou, China. [58]Shanghai Key Laboratory of Anesthesiology and Brain Functional Modulation, Clinical Research Center for Anesthesiology and Perioperative Medicine, Translational Research Institute of Brain and Brain-Like Intelligence, Shanghai Fourth People's Hospital, School of Medicine, Tongji University, Shanghai, China. [59]European Bioinformatics Institute, European Molecular Biology Laboratory, Wellcome Genome Campus, Cambridge, UK. ✉e-mail: e.westhof@ibmc-cnrs.unistra.fr; miao_zhichao@gzlab.ac.cn

Methods

Assessment metrics

The automatic workflow for structural comparisons follows that of the previous rounds of RNA-Puzzles[1–4]. So far, no single or universal metric exists as the primary determinant of the overall accuracy of predictive models. We use a set of metrics to evaluate all models. The r.m.s.d. is used to rank the models. r.m.s.d. is a measure of global topological comparison, but it distributes errors across the entire structure. The r.m.s.d. values are especially useful when they are low. Large values indicate that the prediction is inadequate. We assess the prediction accuracy by comparing each prediction model with the reference structure (when more than one reference structure is present in the experimental dataset, we use the one yielding the lowest r.m.s.d.). Here, we identify meaningful ranges of the r.m.s.d. values for comparing RNA architectures (Fig. 6 and Discussion). Different metrics are used to evaluate the various aspects of the structural predictions as described below.

Procedures to compute r.m.s.d., INF and the DI are provided on the RNA-Puzzles website (www.rnapuzzles.org) and by the RNA-Puzzles toolkit[48,49]. r.m.s.d. is a standard distance measure in comparing 3D structures of biological molecules from a global perspective; however, r.m.s.d., by design, does not consider specific structural features of RNA. Two RNA-based measures have been introduced, INF and DI[6]. To compute the INF, base-pairing and base-stacking interactions are derived from atomic coordinates of both the predicted (*p*) and the reference (*r*) RNA structures using either RNAView[50], MC-Annotate[51] or FR3D[52]. Although checks are carried out with the other tools, the RNA-Puzzles automatic pipeline uses MC-Annotate[51]. Only base pairs with at least two H-bonds between N and O atoms have been considered. These were visually validated and constituted the reference set (Supplementary Table 4). In diagrams, the Leontis–Westhof nomenclature[53] is used for annotating the non-Watson–Crick pairs. Single H-bonded contacts between bases or between bases and phosphate groups have not been considered. Given two sets (*S*) of interactions, *Sr* and *Sp*, obtained for the reference and predicted structure, respectively, one can compare and assess the prediction quality by applying the score originating from binary classification, namely Matthews correlation coefficient (MCC)[6]. Its calculation requires the identification of true positives (TPs; correctly predicted interactions present in *Sr* and *Sp*), false positives (FPs; hallucinated interactions, present only in *Sp*) and false negatives (FNs; interactions missed in prediction, present only in *Sr*). The INF is calculated as the square root of the multiplication of specificity (PPV) and sensitivity (STY), where PPV = |TP|/(|TP| + |FP|) and STY =|TP|/(|TP| + |FN|). INF is a normalized similarity measure taking values in the range [0,1]. INF = 1 means a perfectly preserved interaction network in the predicted model. If there are no common base pairs in *Sr* and *Sp*, then INF = 0. The INF score may be either computed for all base pairs (INF_{all}), or for canonical (INF_{WC}), noncanonical (INF_{nWC}) and stacking ($INF_{stacking}$) interactions independently. The DI is defined as a ratio of r.m.s.d. and INF_{all}. When the interaction network observed in the reference structure is perfectly reproduced in the corresponding predicted model, the DI score is equal to r.m.s.d. Otherwise, the r.m.s.d. value is multiplied by the inverse of the INF_{all} value. The Clash score shows the credibility of the structure in terms of bond distances, angles and stereochemistry (best models have Clash scores close to null)[10].

Modeling methods

Each group can submit up to ten (five after 2018) models per RNA-Puzzle using a single method. The submitted models are named PI-Name_Model-Number. A group can submit models using different approaches or tools to compare their efficacy and accuracy (Supplementary Table 5). Each group is named after the principal investigator (PI) for human-based predictions or after the modeling tool used for automatic web-based predictions. Below the modeling methods used by 15 groups are described (organized by alphabetical order of the PI name). For three groups, the DiMiao group (University of Washington) and two anonymous groups, we could not retrieve more precise methodological information.

Boniecki group

The predictions submitted by M. Boniecki (International Institute of Molecular and Cell Biology in Warsaw) were obtained as a result of simulations using unpublished versions of SimRNA[13,54]. Neither secondary structure predictions nor explicit evolutionary information were considered. Versions of the energy function were obtained based on different decompositions of the total energy. The overall prediction pipeline was similar to a typical prediction scheme using SimRNA: Monte Carlo simulation using the replica-exchange Monte Carlo method and clustering of the results. No method was used to refine the structures. Predictions were essentially obtained without human intervention; no human-assisted modeling stage.

Bujnicki group

The Bujnicki group (International Institute of Molecular and Cell Biology in Warsaw) participated in all the RNA-Puzzles, submitting up to five models both for the webserver and human expert competitions. The webserver models were prepared with SimRNAweb[55], whereas for the human expert models, we employed an array of methods along with human interventions involving research into target RNA sequences and deliberations within the group.

In a typical workflow, the first step was to run literature and sequence similarity searches to find RNA sequences obviously related to the RNA-Puzzle target sequence. If no obvious relative is found, we looked for remotely related (or evolutionarily unrelated, but structurally similar) RNAs using the in-house method PARNASSUS. This facilitates remote homology searches by encoding RNA sequence and secondary structure information in a 20-letter alphabet, which enables the discovery of remotely related RNAs with conserved secondary structures, missed by conventional sequence-based searches. We predicted the secondary structure using in-house meta-predictor MeSSPredRNA (unpublished), and combined it with any information on secondary structure found by literature searches or mapped from the identified RNAs with known structures that could be used as templates. When chemical probing data were available, we used the RNAProbe webserver[56] for secondary structure predictions. If any potentially structurally similar RNA 3D structures were identified, we used them as templates for generating initial 3D models using ModeRNA. For predictions of local 3D structural motifs, we used building blocks from the RNA Bricks database[57]. RNA–ligand complex models were generated with rDock[58] and RNA–protein complexes were modeled with the NPDock workflow[59].

If the initial models of targets were based on templates with very high sequence similarity, we did not modify them extensively, with the exception of a limited final refinement (see below). In all other cases, that is, if the initial models were considered insufficiently reliable or if no comparative models could be generated, we modeled the RNA 3D structures with SimRNA[13,54], using all restraints that could be inferred from the gathered data. For some targets, we experimented with variants of SimRNA with different options, parameters, and extensions, enabling for example, modeling of RNA–small molecule and RNA–protein complexes. Models for submission were selected based on several criteria, including (1) the results of clustering of best-scored conformations (depending on the specific case 1–10% of all conformations generated); typically we considered up to ten largest clusters; (2) the score calculated by SimRNA, comprising RNA energy and the assessment of spatial restraint satisfaction; (3) optionally the score calculated with our in-house tool mqapRNA (unpublished); and (4) visual inspection of the models. We strived to select models that exhibited substantial conformational diversity for the final submission, except in cases of very obvious RNA structures, when the global 3D fold was

predicted accurately beyond any reasonable doubt. If time permitted, we optimized the models for submission using QRNAS[60], to improve the local geometry and remove the clashes.

Chen group

The methodology employed by the Chen group (University of Missouri) encompasses a combination of hierarchical and hybrid approaches to predict RNA 3D structures. For a given RNA sequence, the initial step involves the prediction of two-dimensional (2D) structures. Subsequently, these predicted 2D structures are used for the modeling of the corresponding 3D structures. The Chen group employed two distinct models for 2D structure prediction: Vfold2D[61–64] and VfoldMCPX[65–67]. Vfold2D is a physics-based model able to account for mismatched base pairs while calculating thermodynamic parameters for a variety of loop motifs. VfoldMCPX extends its predictive capacity to RNA complexes consisting of multiple strands. Both Vfold2D and VfoldMCPX demonstrate the ability to predict pseudoknots and to generate suboptimal structures based on base-pairing probabilities; however, both Vfold2D and VfoldMCPX encounter limitations due to the lack of reliable thermodynamic parameters for higher-order structural elements, including loop-kissing motifs and long-range tertiary interactions. To enhance the accuracy of the predictions, we use sequence analysis, based on the PDB[68], Rfam[45] and RNAcentral[45,69] databases and published experimental data. This structural information, like evolutionary and consensus structural data, is employed as folding constraints for the prediction of 2D structures.

Our methodology entails a multistep approach to predict the 3D structures. Starting from the predicted 2D structures, we utilize our template-based 3D structure prediction models, namely Vfold3D[64,70] and VfoldLA[71]. Further refinement of the 3D structures is accomplished through the application of the CG molecular dynamics IsRNA[72,73] and RNAJP[74], which are also guided by the predicted 2D structures. The CG approach is particularly efficient for conformational sampling of large RNAs[74,75]. The final predicted structures are obtained by clustering the low-energy conformations. Our 3D structure prediction modeling programs have several unique features. The CG force field integrated within the IsRNA model takes into consideration both local and nonlocal correlations between various structural degrees of freedom and accounts for the distribution of native and non-native conformations across the energy landscape. In contrast, RNAJP[74] is specifically designed to predict 3D structures for RNAs featuring junctions, with a focus on enhancing global topology sampling. Notably, RNAJP[74] excels in the prediction of RNA junction structures, enabling us to precisely model complex RNA systems that include such junction structures.

The Chen group participated in all the 23 Puzzles. To illustrate our prediction methods, we have chosen four targets that fall into distinct categories: an Aptamer (PZ32), a Viral element (PZ39), a Ribozyme (PZ35) and a Riboswitch (PZ37).

Puzzle 32. The RNA 2D structure of PZ32 was predicted using Vfold2D. The average base-pairing probability for the base pairs in this minimum free energy 2D structure exceeds 88%, indicating thermodynamic stability. Comparison between our prediction and the native 2D structure indicates that our model accurately identified approximately 94% (15 out of 16) of the base pairs, missing only one isolated base pair. The 3D structures were predicted using IsRNA, with the predicted 2D structures serving as constraints. In the fourth model we submitted, we observed coaxially stacked helices flanking the large bulge loop, mirroring the native structure, resulting in the smallest r.m.s.d. of 4.989 Å among all the structures submitted; however, our model failed to capture the base-pairing interactions between the bulge loop and the internal loop.

Puzzle 39. The native 2D structure of PZ39 was predicted by Vfold2D, showing a four-way junction structure with calculated free energy of −42.92 kcal mol^{-1}. Additionally, by conducting sequence analysis[76], we identified a homologous structure (PDB code 1RFR) in the PDB database, which was used to model the fourth helix in this junction structure. The 3D structures were predicted using both IsRNA and RNAJP with the predicted 2D structure as constraints. The primary challenge in predicting the 3D structure of this Puzzle lies in determining the junction topology. Our methods predicted the junction topology and the first model we submitted yields a small r.m.s.d. of 3.959 Å, whereas the best model among all groups achieves a lower r.m.s.d. of 3.383 Å.

Puzzle 35. Sequence analysis suggested the presence of two pseudoknots in the RNA. The incorporation of the structure constraints resulted in an accurate prediction of the whole 2D structure[76,77]. The 3D structures were predicted using IsRNA based on the predicted 2D structure. Our best model exhibits a global resemblance to the native structure, albeit with a slightly higher r.m.s.d. of 6.498 Å compared to the best model among all the groups, which has an r.m.s.d. of 5.982 Å. An incorrectly predicted pseudoknot constraint in the 2D structure led to the local structural deviation.

Puzzle 37. We employed Vfold2D to predict both the pseudoknotted and pseudoknot-free 2D structures for PZ37. Our calculations revealed that the optimal pseudoknotted 2D structure, which includes a pseudoknot formed through base pairing between the large internal loop and the three tail nucleotides at the 3′-end, exhibits significantly lower free energy compared to the most stable pseudoknot-free 2D structure. The predicted pseudoknotted 2D structure closely resembles the native one, with 13 out of 14 base pairs correctly predicted. For the prediction of 3D structures, we utilized IsRNA, taking the 2D structure constraints into account. Our best model displays a global resemblance to the native structure, with the lowest r.m.s.d. of 5.42 Å among all the participating groups. The local structural deviation is attributed to the absence of the G6–C40 base pair.

We acknowledge the limitations of our methods when treating RNA complexes, as seen in PZ26, PZ27 and PZ28, which involve a T-box riboswitch–tRNA complex. Due to the lack of thermodynamic parameters, our 2D models cannot accurately model certain RNA–RNA (tertiary) interactions.

Das group (Rosetta-based approaches FARFAR and SWM, and ARES, co-developed with Dror laboratory)

The Das laboratory (Stanford University) submitted models for the majority of Puzzles Round V. The exceptions are two Puzzles in which the Das laboratory members were involved in experimental structure determination of the target or a near-identical molecule (PZ30, human telomerase; and PZ31, the SARS-CoV-2 frameshift stimulation element) and two Puzzles that were also targets in the CASP15 competition[11] (Puzzles 35 and 36, CPEB ribozymes), for which Das laboratory members served as assessors. For the remaining 17 of 21 Puzzles, the Das laboratory made use of tools developed in the Rosetta3 codebase[78].

FARFAR[79] has been the laboratory's primary RNA modeling method since the beginning of RNA-Puzzles, with some automation piloted in the RNAWorks3D server[4] and several further improvements collected in the FARFAR2 method[80], used in RNA PZ22 and later. For most of the present Puzzles, more than one set of models was submitted, with one set selected manually (typically by R.D. in collaboration with laboratory members, tagged as Das), another selected based on the Rosetta energy (typically tagged as FARFAR2) and other sets selected by scoring from a tensor field network developed by the Dror group, tagged as 'TFN' or by the eventual name of the network, ARES[9]). FARFAR(2) was used to submit at least one set of models for 16 of the 17 RNA-Puzzles for which any models were submitted by the Das laboratory. In addition to the FARFAR-based models, for 8 of the 17 RNA-Puzzles, the Das laboratory submitted models from a different Rosetta-based approach, SWM. This method carries out high-resolution conformational search of loops

or junctions without use of fragments of previous RNA structures, guided by the all-atom Rosetta energy function[81], but its application is restricted to targets where only one such unknown loop or junction needs to be built. For Puzzle 11, our laboratory acquired chemical mapping data and released these data with anonymized sequences to the community in the following entries in the RNA Mapping DataBase[81]: RNAPZ11_STD_0001, DMS, CMCT and the SHAPE modifier 1M7 (ref. 82); RNAPZ11_1M7_0001, RNAPZ11_1M7_0002, RNAPZ11_1M7_0003, for mutate-and-map data with three sets of mutations per nucleotide[83,84]. De-anonymized versions of these datasets are now available at RNAPZ11_STD_0002, RNAPZ11_1M7_0004, RNAPZ11_1M7_0005, RNAPZ11_1M7_0006.

For all RNA-Puzzles to date, including targets for which the most accurate overall model was submitted, the Das laboratory has been able to identify background literature describing the function and, typically, candidate secondary structures or other constraints useful for modeling. For PZ18 (Zika xrRNA), a domain-swapped crystal structure of a different xrRNA served as a template, but expert input was required to inform which regions could be used as templates and which needed to be built de novo with SWM, which was being developed concomitantly with PZ18. For PZ22 (Hatchet ribozyme), secondary structures from RNAfold[85] were refined based on manual inspection of covariance in published sequence alignments. For PZ23 (iMango-III), potential G-quadruplexes as well as the binding site of the ligand were hypothesized after inspection of previously solved Mango aptamers, and these hypotheses were used to seed distinct SWM runs that led to each of the submissions. For PZ24 (VA-I), a pseudoknotted secondary structure had been proposed in the literature and was used to seed FARFAR2 modeling, followed by ARES scoring, which was being developed concomitantly through PZ24–PZ28 in close collaboration with the Dror laboratory. For Puzzles 26–28 (T-box–tRNA complexes), secondary structures, including the set of intermolecular base pairs between the tRNA CAA tail and the T-box, and templates from previously solved fragments of tRNA–T-box complexes were identified manually and used in FARFAR2 modeling, followed by ARES scoring. For PZ34 (methyltransferase ribozyme), special SWM runs were carried out that modeled the RNA with the enzymatic product m^1A at the methylation site, and manual model selection took into consideration the steric accessibility for an exogenous O6-methylguanine as the methyl donor.

Ding group

The Ding group (Clemson University) participated in all rounds, except for PZ27, PZ29 and PZ34. Structures were derived using a multiscale discrete molecular dynamics (DMD) approach[86]. Secondary structures were acquired from consensus results, incorporating homology models from the Rfam database[87] and prediction algorithms such as RNAstructure[88] and mFold[89,90]. CG RNA simulations with temperature replica-exchange DMD were executed using secondary structures as input constraints. Centroid nodes of the ten largest clusters were generated from 10,000 snapshots with the lowest energies in the ensemble produced from CG simulations followed by all-atom DMD simulations for structure refinement.

The Ding group observed that explicitly adding magnesium ions in all-atom simulations improves prediction results by generating more native-like compact conformations. We proposed that optimizing CG simulations might efficiently yield enlarged native-like structure popularities compared to the time-consuming all-atom simulations starting with noncompact RNA molecules. Here, we implemented magnesium ion modeling in CG simulations. The force field between phosphate atoms and magnesium ions was established using the iterative Boltzmann inversion method[91], based on the probability of density as the function of pair distances from all high-resolution RNA molecules in the PDB bank. The addition of 20 mM magnesium ions in the simulation boxes mimicking physiological concentrations successfully created crosslinks between phosphate atoms via binding with RNA molecules, resulting in compact structures. We continuously updated force fields for CG models starting with PZ26. Centroid nodes from several significant clusters from CG simulations followed by rapid all-atom reconstruction led to competitive predictions that performed well in several Puzzles (PZ30, PZ31 and PZ32); however, crosslinks between phosphate beads in CG models could also result in some unphysical over-compact structures dominated as observed in PZ33. To address this, all-atom replica-exchange DMD simulations with explicit magnesium ions modeling were performed, using the most populated structures from CG simulations as initial conformations. Up to ten representative models were generated based on the all-atom simulation structures with the lowest energies for the submitted predictions. Detailed sampling methods can be found in earlier work[4]. For single-chain target PZ39, the lowest backbone r.m.s.d. decreased from 9.0 Å to 6.5 Å after all-atom simulations were performed with the updated workflow. Incorrect secondary structures for several targets, including PZ35, PZ37 and PZ38, suggested that more references of secondary structures should be considered. Although the group ranked third for the multichain target PZ36, large r.m.s.d. values were found, indicating that more efforts should be made to improve predictions of interchain interactions for complex systems. In conclusion, to capture native-like structures, compact conformations need to be generated with correct input constraints of secondary structures as the prerequisite, followed by structure refinement from all-atom simulations for the final submissions.

Dokholyan group

The Dokholyan group (Penn State College of Medicine, Hershey) participated in all Puzzles, submitting five models for each target in the human category. All predictions were carried out using the iFoldRNA program[92–94] and a neural network-based method, epRNA[95,96]. In iFoldRNA, the conformational space of RNA molecules is sampled using CG DMD[86,97] simulations. Representative structures are selected based on energies and, where applicable, additional filters such as the radius of gyration and other experimentally known parameters. RNA nucleotides are represented by three pseudo-atoms corresponding to the base, sugar and phosphate groups in these simulations. Constraints are applied to neighboring beads along the sequence to maintain RNA chain connectivity and local geometry, including covalent bonds, bond angles and dihedral angles. The parameters for bonded interactions are derived from high-resolution RNA structures. Starting from an initial CG RNA model, an all-atom model is reconstructed and further optimized with all-atom DMD simulations. epRNA relies on a convolutional neural network to predict pairwise distances between residues within an RNA molecule. This prediction was accomplished using a recently described smooth parametrization of Euclidean distance matrices. High-accuracy predictions were achieved for RNAs of up to 100 nucleotides in length, in a fraction of a second, marking a 10^7-fold increase in speed compared to existing molecular dynamics-based methods. The conversion from a CG machine-learning output to an all-atom model was executed through DMD with constraints. Secondary structure predictions were obtained using the mFold[89,90] and pKiss webservers. These predictions were subsequently subjected to the iFoldRNA and epRNA programs, resulting in the generation of three models by iFoldRNA and two models by epRNA for each target.

Kollmann group

Dfold (from Kollmann group; Heinrich Heine University of Düsseldorf) is a deep-learning approach to predict 3D folding structures of RNAs from their nucleic acid sequence. It combines a Vector Quantised Variational Autoencoder (VQ-VAE), an autoregressive Deep Generative Model, Monte Carlo Tree Search (MCTS) and a score model to find and rank the most likely folding structures for a given RNA sequence. Training is executed on all available RNAs from the protein database as well as a large corpus of drifted structures augmented from that base set.

To encode 3D RNA structures, Dfold uses a rotational invariant representation that was given by the Euclidean distances between nucleotides followed by a VQ-VAE to compress the Euclidean distances between the selected atoms into three distance classes for each possible nucleotide pair. Hence, the prediction problem is now greatly reduced to the prediction of a distance class map of shape L × L × 3. The autoregressive network learns via the masked pixel objective to map from sequence to distance classes and consists of a deep residual architecture as well as attention layers to further extract information from SHAPE data as well as homologous sequences. For inference Dfold uses MCTS to pixel-wise sample a map of distance classes with the probability values of the autoregressive network. A sampled distance map is ranked by a score network that is based on structures and drifted structures learn to rank them toward minimal energy. The ranked output of distance class maps is calculated back to Euclidean space via the VQ-VA. Thus, Dfold computes an ensemble of ranked tertiary candidate structures.

LCBio group

The Laboratory of Computational Biology (LCBio) group (Nithin group, University of Warsaw) participated in Puzzles P30–P36, and submitted 31 models in the human category. For all the Puzzles in the initial step, we queried Rfam[45] and RNAcentral[69] databases to check for homologous RNA sequences. Simultaneously, the RCSB PDB was searched for 3D structures of homologous RNA molecules. We used ViennaRNA[98], RNAStructure[88], ProbKnot[99], CentroidFold[100], ContraFold[101] and IPknot[102] to predict the secondary structure of the RNA. Additionally, if RNAcentral provided a pre-annotated secondary structure, it was included to enrich the ensemble. We generated a consensus secondary structure using a majority-rule approach. This consensus served as a guide for setting up restraints in 3D structural prediction. For Puzzles PZ35 and PZ36, we additionally used the bifold program from RNAStructure package to predict the secondary structures.

We used the SimRNA program[54,102] for 3D structure modeling. SimRNA was executed with and without secondary structure restraints, using eight independent replica-exchange Monte Carlo simulations, each with ten replicas and 16 million iterations[13]. The lowest-energy structures from the top three clusters were selected for further analysis. In the next step, we refined the models using the QRNAs program[60] to mitigate errors stemming from the initial CG modeling. In the case of Puzzle PZ30, we generated the 3D structure through homology modeling, followed by optimization using QRNAs and ultimately submitted only a single model.

Finally, we conducted molecular dynamics simulation to refine the models, with the exception of PZ30. Molecular dynamics simulations were performed using the Amber 18 package[60,103]. The initial structural configuration for the simulations was established using tleap and housed in a truncated octahedral box with a 10 Å clearance, and solvated using the TIP3P water model[104]. The χOL3 force field[105,106] tailored for RNA was applied throughout the simulations. A two-phase energy minimization was implemented: the first phase involved 10,000 cycles with restraints and was followed by a second phase of 10,000 cycles without restraints. This was followed by heating, density equilibration and short runs of equilibration. The heating was carried out from 100 K to 300 K for 500 ps with restraints on the entire structure and the density equilibration was performed for 500 ps, also with restraints on the entire structure. Equilibration was performed in four distinct steps: three initial steps each lasting 200 ps with restraints on main chain atoms, and a final 2 ns step to ensure full convergence. The production run was initiated with constant pressure boundary conditions (ntb = 2), isotropic position scaling (ntp = 1), and a pressure relaxation time of taup = 2.0 ps. The production simulations were run for 3.7, 0.4, 0.8, 2.4, 0.2 and 0.5 µs for Puzzles PZ31, PZ32, PZ33, PZ34, PZ35 and PZ36, respectively. Particle-mesh Ewald techniques[107] were employed to compute electrostatic interactions, utilizing a 12 Å cutoff for both electrostatic and Lennard–Jones interactions. The NVT ensemble was used during the equilibration steps (ntb = 1), while the production run operated under the NPT ensemble. Sander was utilized for the minimization processes, while the CUDA-enabled PMEMD was used for all subsequent simulation steps[108–110]. Next, the resulting trajectories were clustered via the NMRCLUST algorithm[111] as implemented in UCSF Chimera[112]. The representative frames from the top five clusters were selected as the final models for the submission.

Perez group

The Perez group (University of Florida) uses the MELD integrative approach[113,114] combining Hamiltonian and Temperature replica-exchange molecular dynamics[115] simulations with noisy information coming from server predictions. We used RNAfold for secondary structure prediction[85] and RNAComposer to predict a starting 3D model[116]. Secondary structure predictions were enforced as possible base pairing between bases, with the caveat that only 70% need to be satisfied at any given time. Along the simulation, the subsets of enforced data can change[113] in coherence with detailed balance. MELD uses Bayesian inference to identify the most likely structures and the best interpretation of the original information. The contacts were enforced as flat-bottom harmonic restraints with a force constant of 350 N m^{-1} and a distance of 2.9 Å between heavy atoms of H-bond, as well as a 15 Å between C4s. At high replica indexes, the temperature is high and information is not enforced, favoring unfolded states and broad sampling of the energy landscape. As the replica index decreases the restraints are enforced more strongly, guiding toward folded or misfolded states while the temperature also decreases. Finally, at the lowest temperature replica, the information is enforced strongly and sampled at the lowest temperature; this is the region where we sample conformations with satisfied base pairing. We use hierarchical clustering (ε = 2 Å) to analyze the lowest five replicas to identify structures with higher population. Top clusters were inspected visually, and several models were selected for submission. Contrary to our experience in protein folding[117], the cluster populations for RNA were very low, which will require future work to identify novel clustering algorithms to classify RNA structures from our ensembles. Meld is a plugin to the OpenMM molecular dynamics software and is freely available at https://github.com/maccallumlab/meld. We used the parmBSC1 for nucleic acids[118–120] and the GBNeckNu2 implicit solvent[121,122]. Each simulation was 1.5 µs using 30 replicas and a 4.5-fs timestep. The replicas expand a temperature range between 300 K and 500 K.

SoutheRNA group

The SoutheRNA group (Université Libre de Bruxelles) participated in Puzzles PZ38 and PZ39, submitting five and ten models, respectively, in the human category. The group developed a computational pipeline that performs three steps: collection of RNA data, modeling of the 3D RNA structure and selection/refinement of the obtained 3D structures.

In the first step we predict the RNA secondary structure given the RNA sequences using RNAfold[85]. If the target RNA sequence has a sufficient number of homologs in the RFAM database[87], we align them using Infernal[123]. The resulting multiple sequence alignment (MSA) is used as input of pydca[124], a coevolutionary-based method that identifies pairs of nucleotides that coevolve in the MSA. As these nucleotide pairs are likely to be in spatial proximity in the 3D RNA structure they are used as constrained in the 3D modeling step. When there is an homologous RNA sequence with a known 3D structure deposited in the PDB[125], we extract nucleotide–nucleotide distance constraints from the template to use in the 3D modeling. All the previously collected information (2D structure and spatial constraints) is then used as constraints in the SimRNA modeling algorithm[54], a Monte Carlo-based approach that we employ to explore the RNA conformational space, to cluster the low-energy structures and to select a final set of few hundreds all-atom structures. For each RNA target we run ten simulations of ten replicas

each with 50-M time steps. In the refinement step, we first rescore the few hundred collected SimRNA structures using SPQR[126], which is a nucleotide-level CG model of RNA. As the final predicted structures, we select either the most populated SimRNA cluster representatives and the representatives with the lowest SPQR energy.

Szachniuk group (formerly Adamiak)

The Szachniuk (formerly Adamiak) group (Poznan University of Technology and Institute of Bioorganic Chemistry PAS) participated in all Puzzles, submitting 120 models in the webserver and 122 in the human category. All predictions were made with RNAComposer, which employs a fragment-based assembly approach[12,116].

For webserver predictions, the group developed a fully automated service that runs on several RNAComposer engines. The system can generate the 3D fold(s) from an RNA sequence alone or accompanied by their secondary structures. It is structured as a four-tier application with a workflow consisting of preliminary data processing, prediction of the 3D structure, assessment and prioritization of the resultant 3D models and preparation of submission files dispatched to the task requester. Procedures of the first stage sift through noncanonical base pairs in the input RNA 2D structure, handle multistranded RNAs and interpret pseudoknot data[127]. In the next stage, the system runs several RNA secondary structure predictors to generate a diverse set of unique structures. They are fragmented into structural elements (loops and double- and single-stranded fragments), each of which serves as a search pattern for exploring a database of 3D RNA structures. Up to ten models are assembled from elements that match the patterns. Next-stage procedures evaluate predictions for total energy, gyration radius, INF and Clash score[48,128,129]. Scores are amalgamated to rank models and select the most promising ones for submission.

In the human category, we used additional data sources, including literature and databases such as Rfam[45], RNAloops[45,130] and ONQUADRO[131] to learn from consensus secondary structure or find specific structure motifs to be sewn into the model using the Insert own structure element option[132]. We implemented an algorithm to identify 3D elements that resemble the secondary structure pattern, although not exactly match it. It increased the number of identified 3D structure elements and the diversity of assembled RNA models. The latter were grouped by the OC cluster analysis software. User-defined 3D structure elements, such as cluster centroids, were considered in the updated version of RNAComposer. In the case of multichain targets (PZ22, PZ22dimer, PZ26, PZ27 and PZ28), we experimented with various configurations of chains connected through different linkers. The linkers encompassed elements such as GAAA loop and single-stranded adenine fragments of varying lengths. For PZ31, PZ32, PZ34, PZ38 and PZ39, we employed 100 ns molecular dynamics simulations in explicit solvent, initiating from the RNAComposer-generated models. From these simulations, we judiciously selected cluster centroids representing stable conformations. The ligands were docked in a potentially promising binding place utilizing semi-automatic procedures in AutoDock Vina. In specific instances, manual docking was performed, guided by experimentally resolved structures, as exemplified by our approach in PZ25, wherein the RNA-2′-deoxyguanosine structure (PDB ID 3DS7) was used as a template. In all Puzzles, final models were validated for close atom contacts, bond lengths, angles, planarity, chirality, oligoribonucleotide linkage and entanglements[15,42].

Xiao group

Xiao group (Huazhong University of Science and Technology) applied first traditional methods based on energy minimization such as RNAfold[98] and RNAstructure[88] and deep-learning methods such as SPOT-RNA[133] and our 2dRNA[134] were used to predict candidate secondary structures of the given sequence. Because the 2D structure predicted by deep-learning methods is usually different from that predicted by traditional methods, the prediction results of traditional methods and deep-learning methods were compared respectively, and each centroid structure was selected. On these two structures, 3dRNA/DNA[135,136] was used to predict the tertiary structure. In 3dRNA/DNA, the most suitable template was searched from our RNA tertiary structure templates library[136] for each secondary structure element (SSE), which was decomposed from the secondary structure[135]. If no template was found, the bi-residue method[135,137] was used to build a tertiary template. These templates were then assembled together and optimized by a Monte Carlo simulation-based program[138] with further energy minimization using Amber ff99OL3 force field[106]. For each secondary structure, 10 structures were predicted and the top1 structure of each with the 3 best structures in the other 18 structures selected by 3dRNAscore[139] were chosen as the final prediction. Despite an improved template library and an optimized program to predict constraints, including pseudoknots, the predictions of 3dRNA/DNA in these Puzzles did not rank well. It was discovered that the inadequate prediction ability was caused by the poor handling of multiple loops. Using r.m.s.d. as the standard, the prediction of PZ11 and PZ33 were much better than others, because these two RNA (5LYS and 7ELP) have no multiple loops. The worst prediction of the SSE in each Puzzle is also the multiple loop, especially in PZ34, PZ38 and PZ39.

Xiong group

The Xiong group (University of Science and Technology) participated in Puzzle 39. The predictions were carried out using the BRiQ program with the strategy of motif prediction, assembly and full structure refinement. The secondary structure of PZ39 came from the bpRNA database. According to the secondary structure, this RNA was split into five structure motifs, including three hairpin loops, one interior loop and one four-way junction. These structure motifs were predicted separately using BRiQ prediction program[140], and then assembled into complete structures and finally optimized by BRiQ refinement program. We perform Monte Carlo modeling with a CG potential, named BRIQX_CG to obtain the topology of the RNA structure. And finally, we run full atomic refinement with statistical potential BRIQX_FA. BRIQX potential is derived from statistics of RNA structure database and quantum mechanics calculation. Different from dividing the total energy of the system into the sum of single-variable functions, like bond angle terms, bond length terms, dihedral angle terms, van der Waals terms and electrostatic terms in a molecular force field, BRIQX potential uses multivariable functions to replace single-variable functions to increase accuracy. The CG version of BRIQX potential is more tolerant to bond breaks and steric clashes to make it easier to move across energy barriers. During the sampling in both CG modeling and full atomic refinement stages, the RNA structure is represented by a graph, in which the node is the local frame of a base and the edge is SE(3) transformation of two bases. In a single Monte Carlo move, one edge is changed into a random SE(3) transformation in predefined space. Usually, we need to generate 1,000 models and select the best one.

Yagoub Ali group

The prediction methodology of the Yagoub Ali group (University of São Paulo) is based on the use of Fragment Assembly of RNA (FARNA), which is in the Rosetta software suite. This algorithm assembles pieces of nucleotides, which can vary in length from 1–3 nucleotides, to predict the tertiary structure of RNA. FARNA uses information from existing RNA structures to improve its predictions. This method is referred to as de novo RNA tertiary structure prediction in the Rosetta software suite. The algorithm is based on a Monte Carlo sampling process to minimize energy using Rosetta's low-resolution knowledge-based energy function. Starting from a low-resolution structure, FARFAR produces a high-resolution structure with atomic accuracy and minimizes hydrogen atom clashes. In addition to the canonical RNA base pairing, FARNA can predict noncanonical structures. Users can provide the secondary structure in dot parentheses notation to predict RNA

tertiary structures more accurately. Please note that users must provide the secondary structure for multistranded molecules. Besides the secondary structure, users can optionally give the native structure to accurately predict RNA structure for all types of RNA molecules, that is, single-stranded RNA molecules and multistranded RNA molecules. The current channeling of the FARNA method is limited in its ability to predict the structure of long RNA molecules. For more details about the FARNA method, refer to Alam et al.[141], Watkins et al.[80] and Watkins et al.[142].

Yang group

The Yang group (Shandong University) participated in three Puzzles (PZ37, PZ38 and PZ39). For PZ38 and PZ39, they submitted five models each in the webserver category, while for PZ37, they submitted ten models in the human group category. In general, the Yang group employed an automated deep-learning-based approach, trRosettaRNA[143], to predict the 3D structures. The inputs of trRosettaRNA include the MSA and predicted secondary structure. The MSA is generated using the rMSA tool[144], which iteratively searches against three sequence databases: NCBI nt[145], Rfam[87] and RNAcentral[146]. The secondary structure is predicted by SPOT-RNA[133] from the nucleotide sequence. With these inputs, trRosettaRNA employs a transformer network named RNAformer to predict one-dimensional and 2D geometries, which are then transformed into energy potentials. The folding of the 3D structure is powered by energy minimization, implemented using pyRosetta[147]. For each target, the L-BFGS algorithm is applied to refine 20 randomly initial structures by minimizing the total energy, resulting in 20 refined full-atom decoys. For each RNA-Puzzles target, the five decoys (ten decoys for PZ37) with the lowest total energy were selected as the final submitted predictions. PZ37 and PZ38 were both ligand-binding targets. The predictions made by the Yang group were solely derived from nucleotide sequences, without any consideration of the ligand information or human intervention; however, the automated predictions from the Yang group were competitive to the predictions from leading human expert groups. For these two targets, the Yang group ranked third out of >15 participating groups in terms of the best-submitted models, achieving r.m.s.d. values of 10.3 Å and 8.7 Å for PZ37 and PZ38, respectively. For PZ39, the predictions from Yang group were not accurate, with r.m.s.d. values > 15 Å. The absence of similar sequences or structures from the known RNAs makes it challenging to model this target using a deep-learning-based method. One of the promising directions is to combine deep learning with traditional techniques like fragment assembly and template-based modeling.

Reporting summary

Further information on research design is available in the Nature Portfolio Reporting Summary linked to this article.

Data availability

All the prediction results and codes used are publicly available at www.rnapuzzles.org. Source data are provided with this paper.

Code availability

All metrics used in RNA-Puzzles for the assessments and comparisons of RNA 3D structures are available at https://github.com/RNA-Puzzles/RNA_assessment. Codes to reproduce all figures are available at https://github.com/RNA-Puzzles/RoundV_reproducibility.

References

48. Magnus, M. et al. RNA-Puzzles toolkit: a computational resource of RNA 3D structure benchmark datasets, structure manipulation, and evaluation tools. *Nucleic Acids Res.* **48**, 576–588 (2020).
49. Magnus, M. & Miao, Z. RNA 3D structure comparison Using RNA-Puzzles toolkit. *Methods Mol. Biol.* **2586**, 263–285 (2023).
50. Yang, H. et al. Tools for the automatic identification and classification of RNA base pairs. *Nucleic Acids Res.* **31**, 3450–3460 (2003).
51. Gendron, P., Lemieux, S. & Major, F. Quantitative analysis of nucleic acid three-dimensional structures. *J. Mol. Biol.* **308**, 919–936 (2001).
52. Zirbel, C. L. et al. Identifying novel sequence variants of RNA 3D motifs. *Nucleic Acids Res.* **43**, 7504–7520 (2015).
53. Leontis, N. B. & Westhof, E. Geometric nomenclature and classification of RNA base pairs. *RNA* **7**, 499–512 (2001).
54. Boniecki, M. J. et al. SimRNA: a coarse-grained method for RNA folding simulations and 3D structure prediction. *Nucleic Acids Res.* **44**, e63 (2016).
55. Magnus, M., Boniecki, M. J., Dawson, W. & Bujnicki, J. M. SimRNAweb: a web server for RNA 3D structure modeling with optional restraints. *Nucleic Acids Res.* **44**, W315–W319 (2016).
56. Wirecki, T. K. et al. RNAProbe: a web server for normalization and analysis of RNA structure probing data. *Nucleic Acids Res.* **48**, W292–W299 (2020).
57. Chojnowski, G., Waleń, T. & Bujnicki, J. M. RNA Bricks—a database of RNA 3D motifs and their interactions. *Nucleic Acids Res.* **42**, D123–D131 (2013).
58. Ruiz-Carmona, S. et al. rDock: a fast, versatile and open source program for docking ligands to proteins and nucleic acids. *PLoS Comput. Biol.* **10**, e1003571 (2014).
59. Tuszynska, I., Magnus, M., Jonak, K., Dawson, W. & Bujnicki, J. M. NPDock: a web server for protein–nucleic acid docking. *Nucleic Acids Res.* **43**, W425–W430 (2015).
60. Stasiewicz, J., Mukherjee, S., Nithin, C. & Bujnicki, J. M. QRNAS: software tool for refinement of nucleic acid structures. *BMC Struct. Biol.* **19**, 1–11 (2019).
61. Cheng, Y., Zhang, S., Xu, X. & Chen, S.-J. Vfold2D-MC: a physics-based hybrid model for predicting RNA secondary structure folding. *J. Phys. Chem. B* **125**, 10108–10118 (2021).
62. Cao, S. & Chen, S.-J. Predicting RNA pseudoknot folding thermodynamics. *Nucleic Acids Res.* **34**, 2634–2652 (2006).
63. Cao, S. & Chen, S.-J. Predicting structures and stabilities for H-type pseudoknots with interhelix loops. *RNA* **15**, 696–706 (2009).
64. Xu, X., Zhao, P. & Chen, S.-J. Vfold: a web server for RNA structure and folding thermodynamics prediction. *PLoS ONE* **9**, e107504 (2014).
65. Zhang, S., Cheng, Y., Guo, P. & Chen, S.-J. VfoldMCPX: predicting multistrand RNA complexes. *RNA* **28**, 596–608 (2022).
66. Xu, X. & Chen, S.-J. A method to predict the structure and stability of RNA/RNA complexes. *Methods Mol. Biol.* **1490**, 63–72 (2016).
67. Cao, S., Xu, X. & Chen, S.-J. Predicting structure and stability for RNA complexes with intermolecular loop-loop base-pairing. *RNA* **20**, 835–845 (2014).
68. Berman, H. M. et al. The Protein Data Bank. *Nucleic Acids Res.* **28**, 235–242 (2000).
69. RNAcentral Consortium. RNAcentral 2021: secondary structure integration, improved sequence search and new member databases. *Nucleic Acids Res.* **49**, D212–D220 (2021).
70. Cao, S. & Chen, S.-J. Physics-based de novo prediction of RNA 3D structures. *J. Phys. Chem. B* **115**, 4216–4226 (2011).
71. Xu, X., Zhao, C. & Chen, S.-J. VfoldLA: a web server for loop assembly-based prediction of putative 3D RNA structures. *J. Struct. Biol.* **207**, 235–240 (2019).
72. Zhang, D., Li, J. & Chen, S.-J. IsRNA1: prediction and blind screening of RNA 3D structures. *J. Chem. Theory Comput.* **17**, 1842–1857 (2021).
73. Zhang, D. & Chen, S.-J. IsRNA: an iterative simulated reference state approach to modeling correlated interactions in RNA folding. *J. Chem. Theory Comput.* **14**, 2230–2239 (2018).

74. Li, J. & Chen, S.-J. RNAJP: enhanced RNA 3D structure predictions with non-canonical interactions and global topology sampling. *Nucleic Acids Res.* **51**, 3341–3356 (2023).
75. Li, J. & Chen, S.-J. RNA 3D structure prediction using coarse-grained models. *Front. Mol. Biosci.* **8**, 720937 (2021).
76. Glenet, M. et al. Structures and functions of viral 5′ non-coding genomic RNA domain-I in group-B enterovirus infections. *Viruses* **12**, 919 (2020).
77. Li, J., Zhang, S. & Chen, S.-J. Advancing RNA 3D structure prediction: exploring hierarchical and hybrid approaches in CASP15. *Proteins* **91**, 1779–1789 (2023).
78. Leaver-Fay, A. et al. ROSETTA3: an object-oriented software suite for the simulation and design of macromolecules. *Methods Enzymol.* **487**, 545–574 (2011).
79. Das, R., Karanicolas, J. & Baker, D. Atomic accuracy in predicting and designing noncanonical RNA structure. *Nat. Methods* **7**, 291–294 (2010).
80. Watkins, A. M., Rangan, R. & Das, R. FARFAR2: improved de novo rosetta prediction of complex global RNA folds. *Structure* **28**, 963–976.e6 (2020).
81. Watkins, A. M. et al. Blind prediction of noncanonical RNA structure at atomic accuracy. *Sci. Adv.* **4**, eaar5316 (2018).
82. Cordero, P., Kladwang, W., VanLang, C. C. & Das, R. Quantitative dimethyl sulfate mapping for automated RNA secondary structure inference. *Biochemistry* **51**, 7037–7039 (2012).
83. Cordero, P., Kladwang, W., VanLang, C. C. & Das, R. The mutate-and-map protocol for inferring base pairs in structured RNA. *Methods Mol. Biol.* **1086**, 53–77 (2014).
84. Tian, S. & Das, R. Primerize-2D: automated primer design for RNA multidimensional chemical mapping. *Bioinformatics* **33**, 1405–1406 (2017).
85. Gruber, A. R., Lorenz, R., Bernhart, S. H., Neuböck, R. & Hofacker, I. L. The Vienna RNA websuite. *Nucleic Acids Res.* **36**, W70–W74 (2008).
86. Ding, F. et al. Ab initio RNA folding by discrete molecular dynamics: from structure prediction to folding mechanisms. *RNA* **14**, 1164–1173 (2008).
87. Griffiths-Jones, S., Bateman, A., Marshall, M., Khanna, A. & Eddy, S. R. RFAM: an RNA family database. *Nucleic Acids Res.* **31**, 439–441 (2003).
88. Reuter, J. S. & Mathews, D. H. RNAstructure: software for RNA secondary structure prediction and analysis. *BMC Bioinform.* **11**, 129 (2010).
89. Zuker, M. Mfold web server for nucleic acid folding and hybridization prediction. *Nucleic Acids Res.* **31**, 3406–3415 (2003).
90. Janssen, S. & Giegerich, R. The RNA shapes studio. *Bioinformatics* **31**, 423–425 (2014).
91. Reith, D., Pütz, M. & Müller-Plathe, F. Deriving effective mesoscale potentials from atomistic simulations. *J. Comput. Chem.* **24**, 1624–1636 (2003).
92. Sharma, S., Ding, F. & Dokholyan, N. V. iFoldRNA: three-dimensional RNA structure prediction and folding. *Bioinformatics* **24**, 1951–1952 (2008).
93. Krokhotin, A., Houlihan, K. & Dokholyan, N. V. iFoldRNA v2: folding RNA with constraints. *Bioinformatics* **31**, 2891–2893 (2015).
94. Wang, J. et al. Limits in accuracy and a strategy of RNA structure prediction using experimental information. *Nucleic Acids Res.* **47**, 5563–5572 (2019).
95. Sha, C. M., Wang, J. & Dokholyan, N. V. Predicting 3D RNA structure from solely the nucleotide sequence using Euclidean distance neural networks. *Biophys. J.* **122**, 444a (2023).
96. Sha, C. M., Wang, J. & Dokholyan, N. V. Predicting 3D RNA structure from the nucleotide sequence using Euclidean neural networks. *Biophys. J.* **123**, 2671–2681 (2024).
97. Proctor, E. A., Ding, F. & Dokholyan, N. V. Discrete molecular dynamics. *Wiley Interdiscip. Rev. Comput. Mol. Sci.* **1**, 80–92 (2011).
98. Lorenz, R. et al. ViennaRNA package 2.0. *Algorithms Mol. Biol.* **6**, 26 (2011).
99. Bellaousov, S. & Mathews, D. H. ProbKnot: fast prediction of RNA secondary structure including pseudoknots. *RNA* **16**, 1870–1880 (2010).
100. Sato, K., Hamada, M., Asai, K. & Mituyama, T. CENTROIDFOLD: a web server for RNA secondary structure prediction. *Nucleic Acids Res.* **37**, W277–W280 (2009).
101. Do, C. B., Woods, D. A. & Batzoglou, S. CONTRAfold: RNA secondary structure prediction without physics-based models. *Bioinformatics* **22**, e90–e98 (2006).
102. Sato, K., Kato, Y., Hamada, M., Akutsu, T. & Asai, K. IPknot: fast and accurate prediction of RNA secondary structures with pseudoknots using integer programming. *Bioinformatics* **27**, i85–i93 (2011).
103. Salomon-Ferrer, R., Case, D. A. & Walker, R. C. An overview of the Amber biomolecular simulation package. *Wiley Interdiscip. Rev. Comput. Mol. Sci.* **3**, 198–210 (2013).
104. Jorgensen, W. L., Chandrasekhar, J., Madura, J. D., Impey, R. W. & Klein, M. L. Comparison of simple potential functions for simulating liquid water. *J. Chem. Phys.* **79**, 926–935 (1983).
105. Banáš, P. et al. Performance of molecular mechanics force fields for RNA simulations: stability of UUCG and GNRA hairpins. *J. Chem. Theory Comput.* **6**, 3836–3849 (2010).
106. Zgarbová, M. et al. Refinement of the Cornell et al. nucleic acids force field based on reference quantum chemical calculations of glycosidic torsion profiles. *J. Chem. Theory Comput.* **7**, 2886–2902 (2011).
107. Essmann, U. et al. A smooth particle mesh Ewald method. *J. Chem. Phys.* **103**, 8577–8593 (1995).
108. Salomon-Ferrer, R., Götz, A. W., Poole, D., Le Grand, S. & Walker, R. C. Routine microsecond molecular dynamics simulations with AMBER on GPUs. 2. Explicit solvent particle mesh Ewald. *J. Chem. Theory Comput.* **9**, 3878–3888 (2013).
109. Götz, A. W. et al. Routine microsecond molecular dynamics simulations with AMBER on GPUs. 1. Generalized Born. *J. Chem. Theory Comput.* **8**, 1542–1555 (2012).
110. Le Grand, S., Götz, A. W. & Walker, R. C. SPFP: speed without compromise—A mixed precision model for GPU accelerated molecular dynamics simulations. *Comput. Phys. Commun.* **184**, 374–380 (2013).
111. Kelley, L. A., Gardner, S. P. & Sutcliffe, M. J. An automated approach for clustering an ensemble of NMR-derived protein structures into conformationally related subfamilies. *Protein Eng.* **9**, 1063–1065 (1996).
112. Pettersen, E. F. et al. UCSF Chimera–a visualization system for exploratory research and analysis. *J. Comput. Chem.* **25**, 1605–1612 (2004).
113. MacCallum, J. L., Perez, A. & Dill, K. A. Determining protein structures by combining semireliable data with atomistic physical models by Bayesian inference. *Proc. Natl Acad. Sci. USA* **112**, 6985–6990 (2015).
114. Perez, A., MacCallum, J. L. & Dill, K. A. Accelerating molecular simulations of proteins using Bayesian inference on weak information. *Proc. Natl Acad. Sci. USA* **112**, 11846–11851 (2015).
115. Sugita, Y. & Okamoto, Y. Replica-exchange molecular dynamics method for protein folding. *Chem. Phys. Lett.* **314**, 141–151 (1999).
116. Popenda, M. et al. Automated 3D structure composition for large RNAs. *Nucleic Acids Res.* **40**, e112 (2012).
117. Perez, A., Morrone, J. A., Brini, E., MacCallum, J. L. & Dill, K. A. Blind protein structure prediction using accelerated free-energy simulations. *Sci. Adv.* **2**, e1601274 (2016).

118. Cheatham, T. E. 3rd, Cieplak, P. & Kollman, P. A. A modified version of the Cornell et al. force field with improved sugar pucker phases and helical repeat. *J. Biomol. Struct. Dyn.* **16**, 845–862 (1999).
119. Ivani, I. et al. Parmbsc1: a refined force field for DNA simulations. *Nat. Methods* **13**, 55–58 (2016).
120. Pérez, A. et al. Refinement of the AMBER force field for nucleic acids: improving the description of alpha/gamma conformers. *Biophys. J.* **92**, 3817–3829 (2007).
121. Nguyen, H., Pérez, A., Bermeo, S. & Simmerling, C. Refinement of generalized Born implicit solvation parameters for nucleic acids and their complexes with proteins. *J. Chem. Theory Comput.* **11**, 3714–3728 (2015).
122. Nguyen, H., Roe, D. R. & Simmerling, C. Improved generalized Born solvent model parameters for protein simulations. *J. Chem. Theory Comput.* **9**, 2020–2034 (2013).
123. Nawrocki, E. P. & Eddy, S. R. Infernal 1.1: 100-fold faster RNA homology searches. *Bioinformatics* **29**, 2933–2935 (2013).
124. Zerihun, M. B., Pucci, F., Peter, E. K. & Schug, A. pydca v1.0: a comprehensive software for direct coupling analysis of RNA and protein sequences. *Bioinformatics* **36**, 2264–2265 (2020).
125. Berman, H. M. et al. The Protein Data Bank. *Acta Crystallogr. D Biol. Crystallogr.* **58**, 899–907 (2002).
126. Poblete, S., Bottaro, S. & Bussi, G. A nucleobase-centered coarse-grained representation for structure prediction of RNA motifs. *Nucleic Acids Res.* **46**, 1674–1683 (2018).
127. Antczak, M. et al. New algorithms to represent complex pseudoknotted RNA structures in dot-bracket notation. *Bioinformatics* **34**, 1304–1312 (2018).
128. Lukasiak, P. et al. RNAlyzer–novel approach for quality analysis of RNA structural models. *Nucleic Acids Res.* **41**, 5978–5990 (2013).
129. Szachniuk, M. RNApolis: computational platform for RNA structure analysis. *Found. Comput. Decision Sci.* **44**, 241–257 (2019).
130. Wiedemann, J. et al. RNAloops: a database of RNA multiloops. *Bioinformatics* **38**, 4200–4205 (2022).
131. Zok, T. et al. ONQUADRO: a database of experimentally determined quadruplex structures. *Nucleic Acids Res.* **50**, D253–D258 (2022).
132. Antczak, M. et al. New functionality of RNAComposer: an application to shape the axis of miR160 precursor structure. *Acta Biochim. Pol.* **63**, 737–744 (2016).
133. Singh, J., Hanson, J., Paliwal, K. & Zhou, Y. RNA secondary structure prediction using an ensemble of two-dimensional deep neural networks and transfer learning. *Nat. Commun.* **10**, 5407 (2019).
134. Mao, K., Wang, J. & Xiao, Y. Length-dependent deep learning model for RNA secondary structure prediction. *Molecules* **27**, 1030 (2022).
135. Zhao, Y. et al. Automated and fast building of three-dimensional RNA structures. *Sci. Rep.* **2**, 734 (2012).
136. Zhang, Y., Wang, J. & Xiao, Y. 3dRNA: building RNA 3D structure with improved template library. *Comput. Struct. Biotechnol. J.* **18**, 2416–2423 (2020).
137. Wang, J., Wang, J., Huang, Y. & Xiao, Y. 3dRNA v2.0: an updated web server for RNA 3D structure prediction. *Int. J. Mol. Sci.* **20**, 4116 (2019).
138. Wang, J. et al. Optimization of RNA 3D structure prediction using evolutionary restraints of nucleotide-nucleotide interactions from direct coupling analysis. *Nucleic Acids Res.* **45**, 6299–6309 (2017).
139. Wang, J., Zhao, Y., Zhu, C. & Xiao, Y. 3dRNAscore: a distance and torsion angle dependent evaluation function of 3D RNA structures. *Nucleic Acids Res.* **43**, e63 (2015).
140. Chen, K., Zhou, Y., Wang, S. & Xiong, P. RNA tertiary structure modeling with BRiQ potential in CASP15. *Proteins* **91**, 1771–1778 (2023).
141. Alam, T. et al. FARNA: knowledgebase of inferred functions of non-coding RNA transcripts. *Nucleic Acids Res.* **45**, 2838–2848 (2016).
142. Watkins, A. M. & Das, R. RNA 3D Modeling with FARFAR2, Online. *Methods Mol. Biol.* **2586**, 233–249 (2023).
143. Wang, W. et al. trRosettaRNA: automated prediction of RNA 3D structure with transformer network. *Nat. Commun.* **14**, 7266 (2023).
144. Zhang, C., Zhang, Y. & Pyle, A. M. rMSA: a sequence search and alignment algorithm to improve RNA structure modeling. *J. Mol. Biol.* **435**, 167904 (2023).
145. Sayers, E. W. et al. Database resources of the national center for biotechnology information. *Nucleic Acids Res.* **50**, D20–D26 (2022).
146. The RNAcentral Consortium. RNAcentral: a hub of information for non-coding RNA sequences. *Nucleic Acids Res.* **47**, D221–D229 (2019).
147. Chaudhury, S., Lyskov, S. & Gray, J. J. PyRosetta: a script-based interface for implementing molecular modeling algorithms using Rosetta. *Bioinformatics* **26**, 689–691 (2010).

Acknowledgements

Z.M. is supported by Major Projects of Guangzhou National Laboratory (grant no. GZNL2023A01006, GZNL2024A01002, SRPG22-003, SRPG22-006, SRPG22-007, HWYQ23-003 and YW-YFYJ0102), the Natural Science Foundation of China (32270707) and the National Key R&D Programs of China (2023YFF1204700, 2023YFF1204701, 2021YFF1200900 and 2021YFF1200903). This work is part of the ITI 2021–2028 program and supported by IdEx Unistra (ANR-10-IDEX-0002 to E.W.), SFRI-STRAT'US project (ANR-20-SFRI-0012) and EUR IMCBio (IMCBio ANR-17-EURE-0023 to E.W.) under the framework of the French Investments for the Future Program. E.W. also acknowledges support from Wenzhou Institute, University of Chinese Academy of Sciences (WIUCASQD2024002). A.P. is supported by an NSF CAREER award CHE-2235785. M.A., M.P., J.S., T.Z. and M.S. are supported by the National Science Centre, Poland (2019/35/B/ST6/03074 to M.S.), the statutory funds of IBCH PAS and Poznan University of Technology. N.V.D. is supported by the National Institutes of Health (NIH) grants 1R35 GM134864 and the Passan Foundation. R.D. is supported by Stanford Bio-X (to R.D., R.O.D., R.C.K. and S.E.); Stanford Gerald J. Lieberman Fellowship (to R.R.); the NIH (R21 CA219847 and R35 GM122579 to R.D.), the Howard Hughes Medical Institute (to R.D.); Consejo Nacional de Ciencia y Tecnología CONACyT Fellowship 312765 (to P.C.); the Ruth L. Kirschstein National Research Service Award Postdoctoral Fellowships GM112294 (to J.D.Y.); National Science Foundation Graduate Research Fellowships (to R.J.L.T. and R.R.); the National Library of Medicine T15 Training Grant (NLM T15007033 to K.A.C.); and the US Department of Energy, Office of Science Graduate Student Research program (to R.J.L.T.). R.O.D. is supported by the US Department of Energy, Office of Science, Scientific Discovery through Advanced Computing (SciDAC) program and Intel. D.K. is supported by the NSF CAREER award MCB-2236996 and start-up, SURFF and START awards from the University of Maryland Baltimore County (to D.K.) and partly by the NIH T32 grant GM066706 (to N.K.D.). L.H. is supported by National Natural Science Foundation of China (32171191), Guangdong Science and Technology Department (2022A1515010328, 2023B1212060013 and 2020B1212030004) and Fundamental Research Funds for the Central Universities, Sun Yat-sen University (23ptpy41). J.Z. is supported by the Intramural Research Program of the NIH, the National Institute of Diabetes and Digestive and Kidney Diseases (ZIADK075136 to J.Z.), and an NIH Deputy Director for Intramural Research Challenge Award to J.Z. A.F.D. is supported, in part, by the intramural program of the National Heart, Lung and Blood Institute, NIH, USA. A.R. is supported by grants from the Natural Science Foundation of China (32325029, 32022039, 91940302 and 91640104) and the National Key Research and Development Project of China (2021YFC2300300 and 2023YFC2604300). C.N. and M.K. acknowledge funding from the National Science Centre,

Poland (OPUS 2019/33/B/NZ2/02100). S.P.P. acknowledges funding from the National Science Centre, Poland (OPUS 2020/39/B/NZ2/01301). S.K. acknowledges funding from the National Science Centre, Poland (Sheng 2021/40/Q/NZ2/00078). C.N. acknowledge Polish high-performance computing infrastructure PLGrid (HPC Centers: PCSS, ACK Cyfronet AGH, CI TASK, WCSS) for providing computer facilities and support within the computational grants PLG/2022/016043, PLG/2022/015327 and PLG/2020/013424. J.Y. is supported in part by the National Natural Science Foundation of China (NSFC T2225007). B.M. is supported by the Interdisciplinary Thematic Institute IMCBio, as part of the ITI 2021-2028 program at the University of Strasbourg, CNRS and Inserm, by IdEx Unistra (ANR-10-IDEX-0002) and EUR (IMCBio ANR-17-EUR-0023), under the framework of the French Investments Program for the Future. R.T.B. is supported by a grant from the NIH (R01 GM073850). J.M.B. is supported by the National Science Centre in Poland (NCN grants 2017/26/A/NZ1/01083 to J.M.B., 2021/43/D/NZ1/03360 to S.M., 2020/39/B/NZ2/03127 to F.S. and 2020/39/D/NZ2/02837 to T.K.W.). E.F.B. was additionally supported by a European Molecular Biology Organization fellowship (ALTF 525-2022). J.M.B. acknowledge Poland high-performance computing Infrastructure PLGrid (HPC Centers: ACK Cyfronet AGH, PCSS, CI TASK, WCSS) for providing computer facilities and support within the computational grant PLG/2023/016080. F.D. is supported by NIH R35GM145409 and P20GM121342. S.J.C. is supported by the NIH under grant R35-GM134919. J.W. is supported by the Penn State College of Medicine's Artificial Intelligence and Biomedical Informatics Program. M.J.B. is supported by the Polish National Science Center Poland (grant 2016/23/B/ST6/03433). Predictions were performed using computational resources of the Interdisciplinary Centre for Mathematical and Computational Modelling of the University of Warsaw (grant G66-9). T.H.D.N. is supported by UKRI–Medical Research Council grant MC_UP_1201/19. S.P. is supported by the Fondecyt Regular project no. 1231071 and Centro Ciencia & Vida, FB210008, Financiamiento Basal para Centros Científicos y Tecnológicos de Excelencia de ANID. H.V.G. acknowledges financial support from the Ramón y Cajal grant no. RYC2022-038082-I and CEX2023-001263-S.

Author contributions

E.W. conceived of and supervised the project, coordinated the collaboration, analyzed the results and wrote the paper. Z.M. supervised the project, organized the predictions, coordinated the collaboration, analyzed the results, built the website and wrote the paper. F.B. analyzed the results, visualized the data, produced and checked figures and tables, maintained the website and checked the paper. M.A. and T.Z. analyzed all the predictions for entanglements. T.Z. performed the study of PZ23 models to diagnose problems in predicting the quadruplex structure. All other contributing authors either worked and produced the experimental structures or participated and contributed to the predictions of the structures. Each modeling group wrote the prediction methods that they had been using. All authors had the possibility to contribute to the text, figures and tables.

Competing interests

The authors declare no competing interests.

Additional information

Extended data is available for this paper at https://doi.org/10.1038/s41592-024-02543-9.

Supplementary information The online version contains supplementary material available at https://doi.org/10.1038/s41592-024-02543-9.

Correspondence and requests for materials should be addressed to Eric Westhof or Zhichao Miao.

Peer review information *Nature Methods* thanks Liang Huang, Qiangfeng Cliff Zhang, and the other, anonymous, reviewer(s) for their contribution to the peer review of this work. Primary Handling Editor: Rita Strack, in collaboration with the *Nature Methods* team. Peer reviewer reports are available.

https://doi.org/10.1038/s41592-024-02543-9

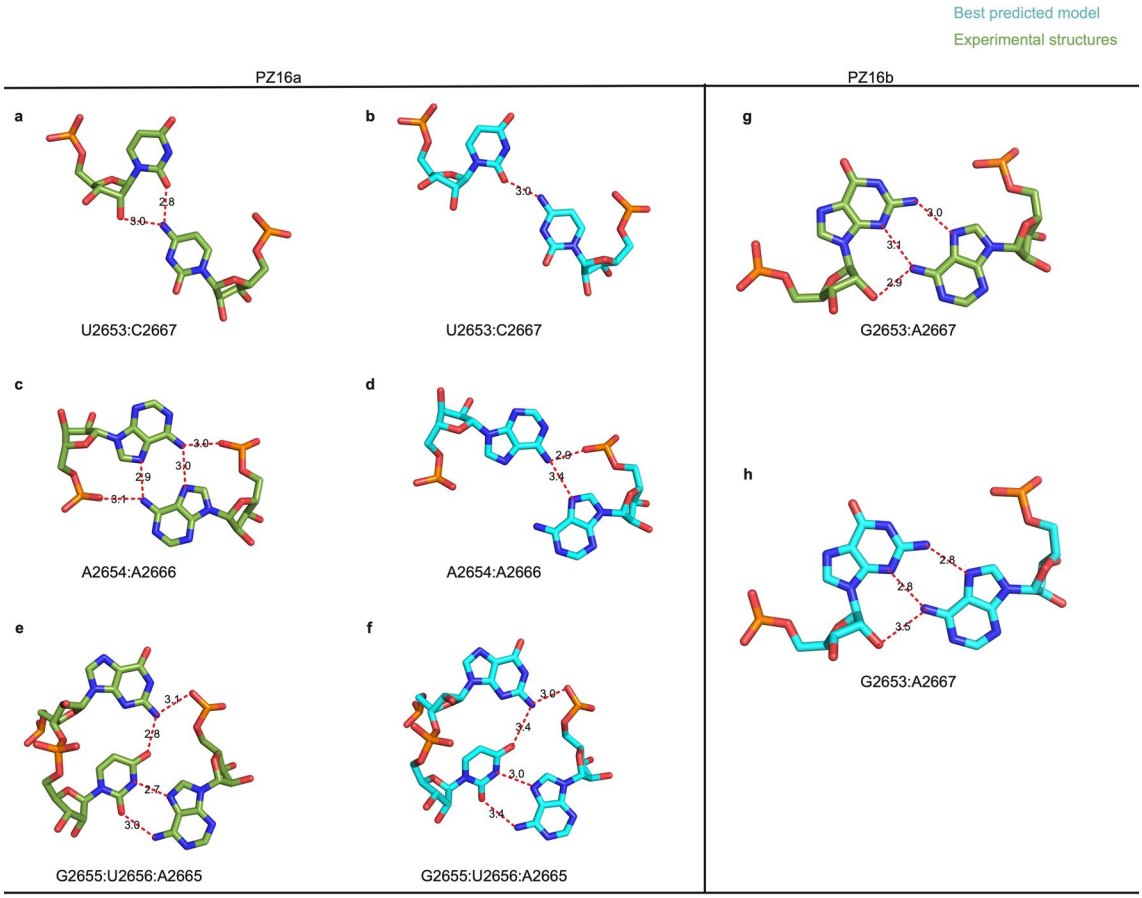

Extended Data Fig. 1 | Comparisons of key non-Watson–Crick pairs between the experimental and best-predicted structures in PZ16a and PZ16b. (**a**–**e**) Non-Watson–Crick pairs in the experimental structure of PZ16a (PDB id: 6y0y). (**b**–**f**) Best-predicted non-Watson–Crick pairs for PZ16a (RNAComposerAS1_3, r.m.s.d. = 1.2 Å). (**g**) Non-Watson–Crick pairs in the experimental structure of PZ16b (PDB id: 6y0t). (**h**) Best-predicted non-Watson–Crick pairs for PZ16b (RNAComposerAS2_1, r.m.s.d. = 1.3 Å).

https://doi.org/10.1038/s41592-024-02543-9

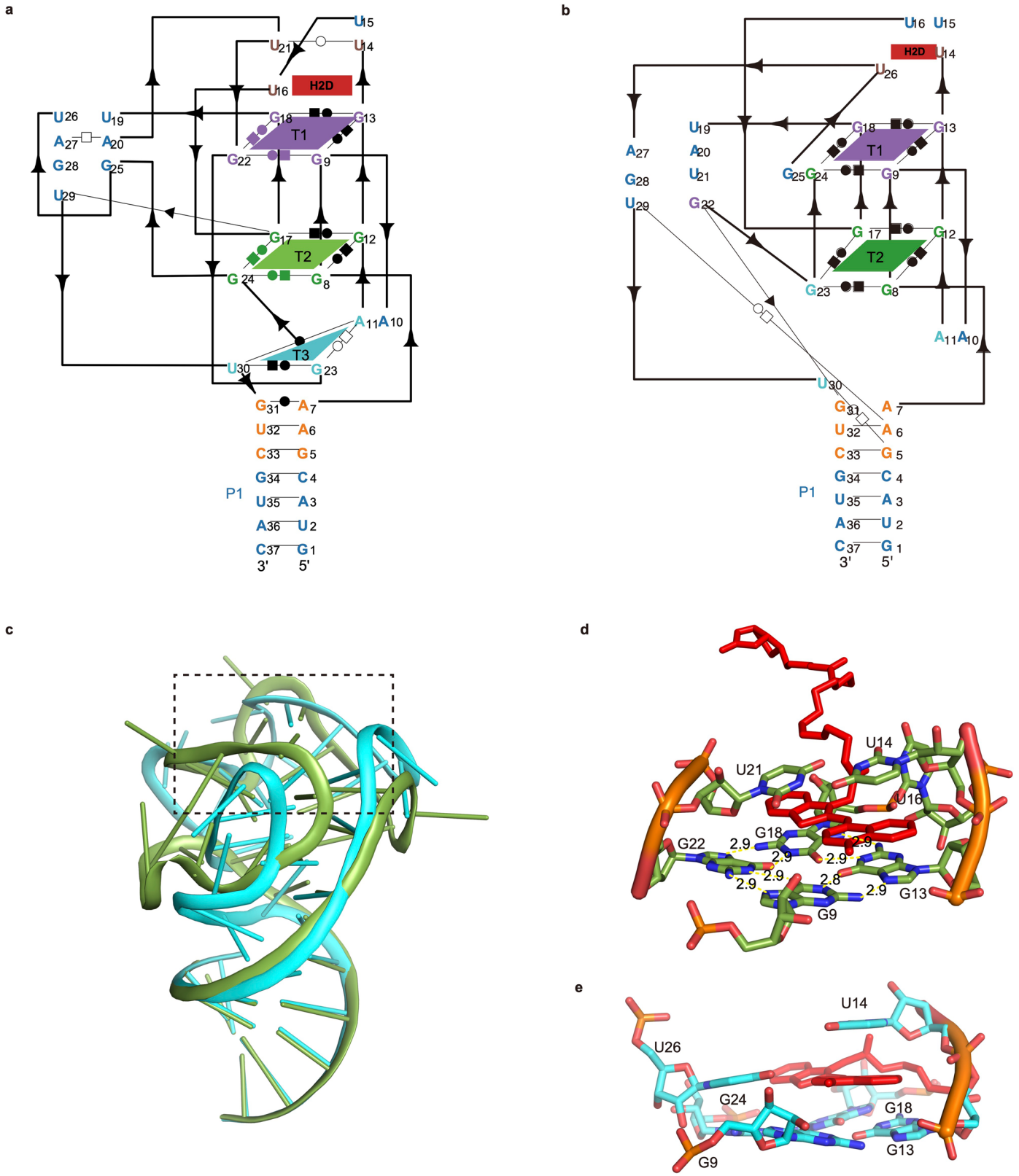

Extended Data Fig. 2 | Detailed analysis of PZ23, the Mango Aptamer. (**a**) Diagrams of the interaction contacts for the experimental structure (PDB ID: 6e8u) and (**b**) for the best-predicted structure (DAS_7, r.m.s.d. = 8.1 Å). The position of the ligand, thiazole orange linked to Biotin (H2D), is shown in a red rectangle. See Supplementary Fig. 5(i) for more detailed descriptions of the unusual quadruplex structure of PZ23. (**c**) Global overlay of the target (in green) with the best-predicted model (in blue: Das_7)(global r.m.s.d. without the ligand: 8.1 Å; INFnwc: 0.45). The region within the dashed box is highlighted in (**d**) and (**e**) where are shown respectively the structural environment around the bound ligand (in red) within the target (in green) and the best-predicted model (in blue).

https://doi.org/10.1038/s41592-024-02543-9

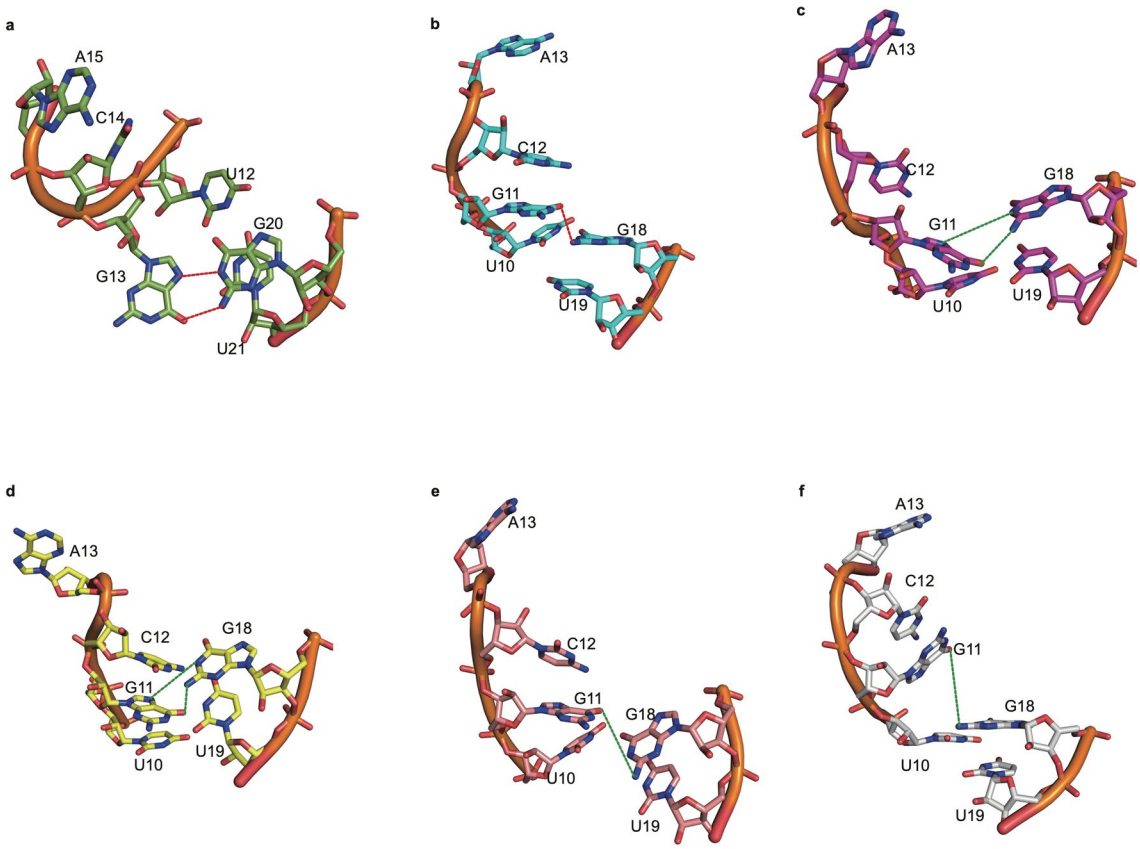

Extended Data Fig. 3 | Detailed analysis of predictive models for Viral elements. (**a**–**f**) The results of the 12–21 base pair in the crystal structure (PDB id:7mlx) and the top 5 predicted structures of PZ31 (**b**) Dokholyan_2, r.m.s.d. = 4.80 Å, (**c**) Dokholyan_1, r.m.s.d. = 4.96 Å, (**d**) Chen_7, r.m.s.d. = 5.17 Å, (**e**) Chen_5, r.m.s.d. = 5.42 Å, (**f**) Bujnicki_2, r.m.s.d. = 5.45 Å). The H-bonds are color-coded as a function of length: < 4.0 Å in red and beyond 5 Å in green. Two residues are missing at the 5′-end of the modeled sequences.

https://doi.org/10.1038/s41592-024-02543-9

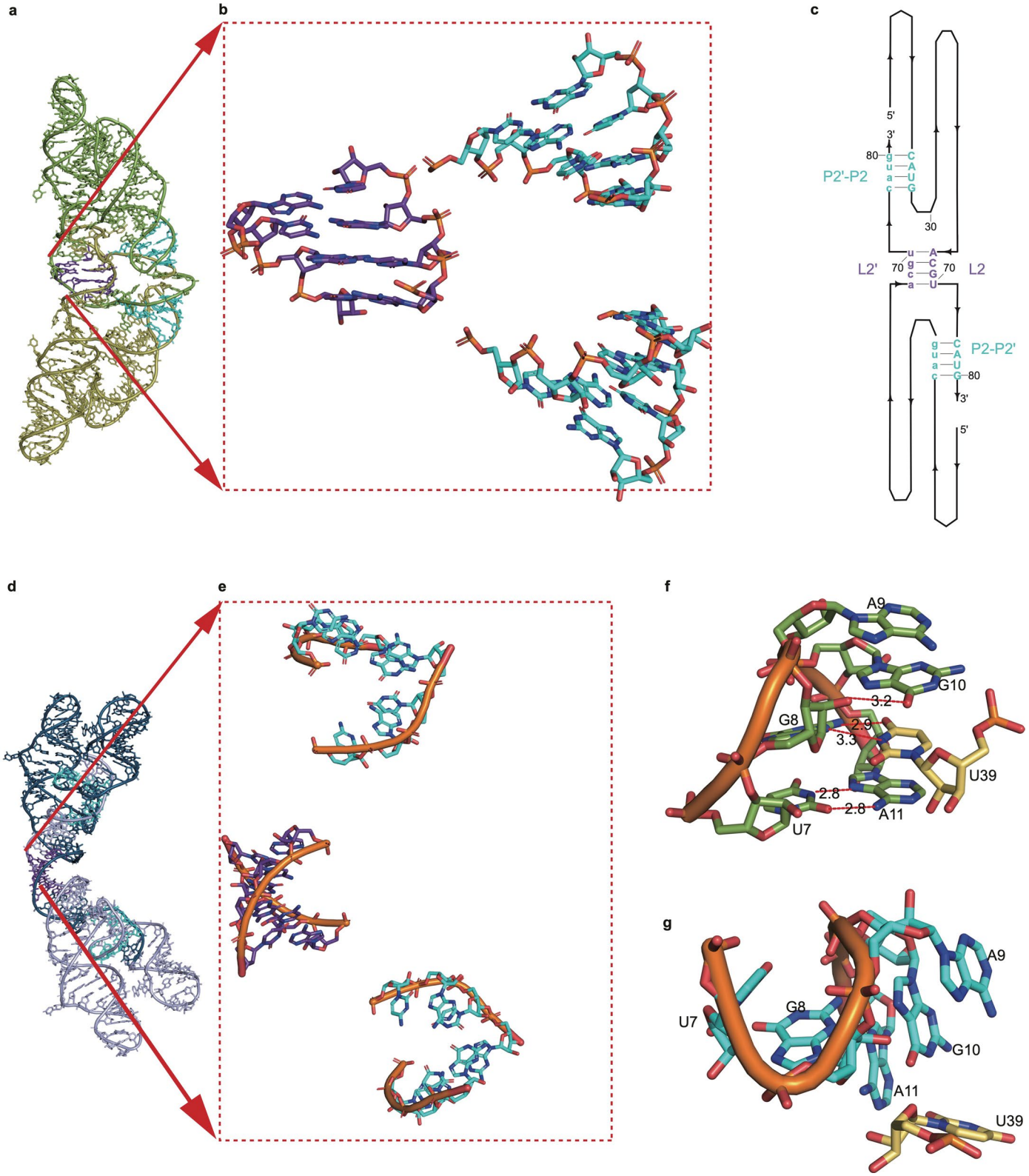

Extended Data Fig. 4 | Detailed analysis of predictive models for Ribozymes. (**a**) Experimental structure of PZ22dimer (PDB ID: 6jq5). (**b**) Experimental dimer region. (**c**) Simplified secondary structure diagram focusing on the intermolecular helices formed in the dimer. (**d**,**e**) Predicted PZ22dimer structure (Adamiak_5, r.m.s.d. = 20.2 Å), (**d**) Tertiary structure, (**e**) Dimer region, and (**f**,**g**) Comparison of key regions between the experimental and predicted structures (Das_5, r.m.s.d. = 10.7 Å) of PZ22 (5′-U7GAGA11-3′ + U39).

https://doi.org/10.1038/s41592-024-02543-9

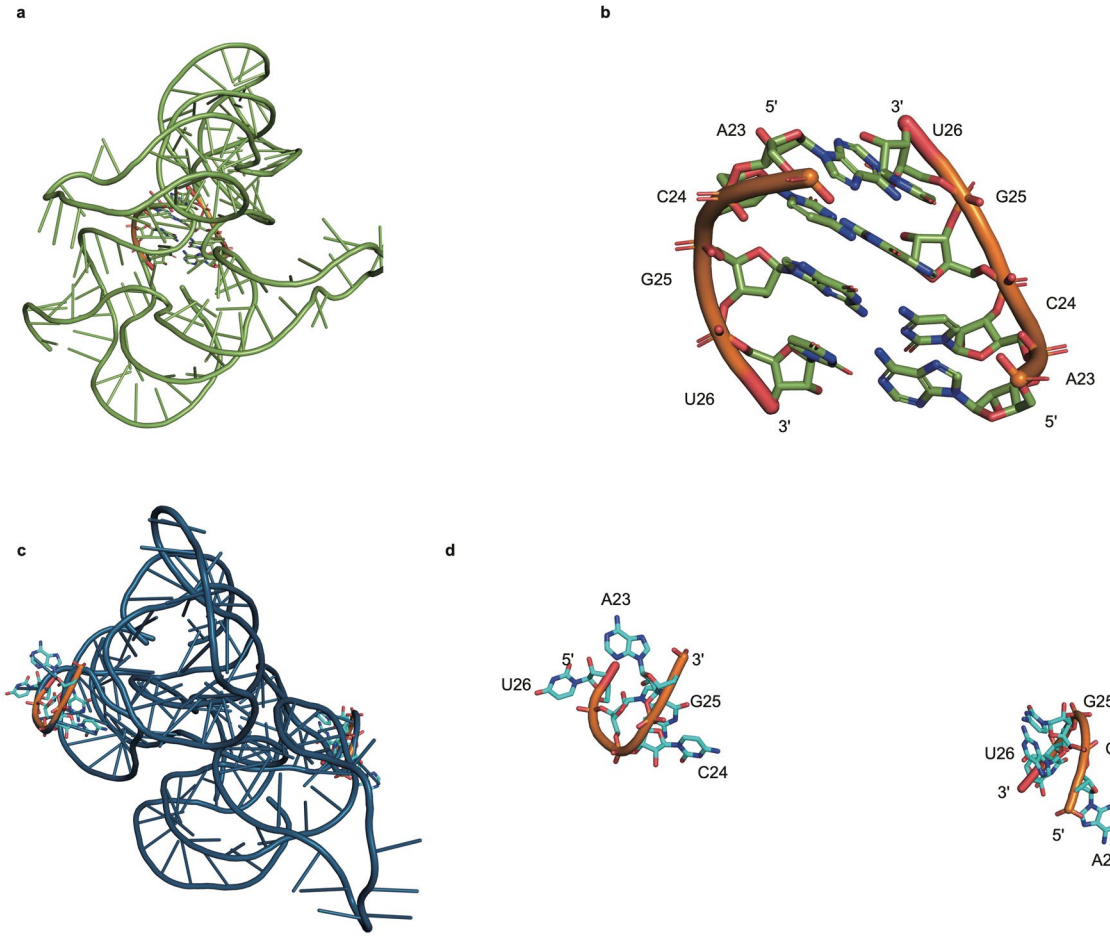

Extended Data Fig. 5 | Detailed analysis of PZ36, the dimer region of the Chimpanzee CPEB3 HDV-like ribozyme. The figures illustrate differences in the dimer region between the crystal structure (PDB ID: 7qr3) and the predicted structures (Szachniuk_4, r.m.s.d. = 21.2 Å). (**a**) the crystal structure of the dimer. (**b**) the helical region key to the formation of the dimer. (**c**,**d**) the same for the best-predicted model (Szachniuk_4, r.m.s.d. = 21.2 Å) where the two strands that should pair are far away from each other.

https://doi.org/10.1038/s41592-024-02543-9

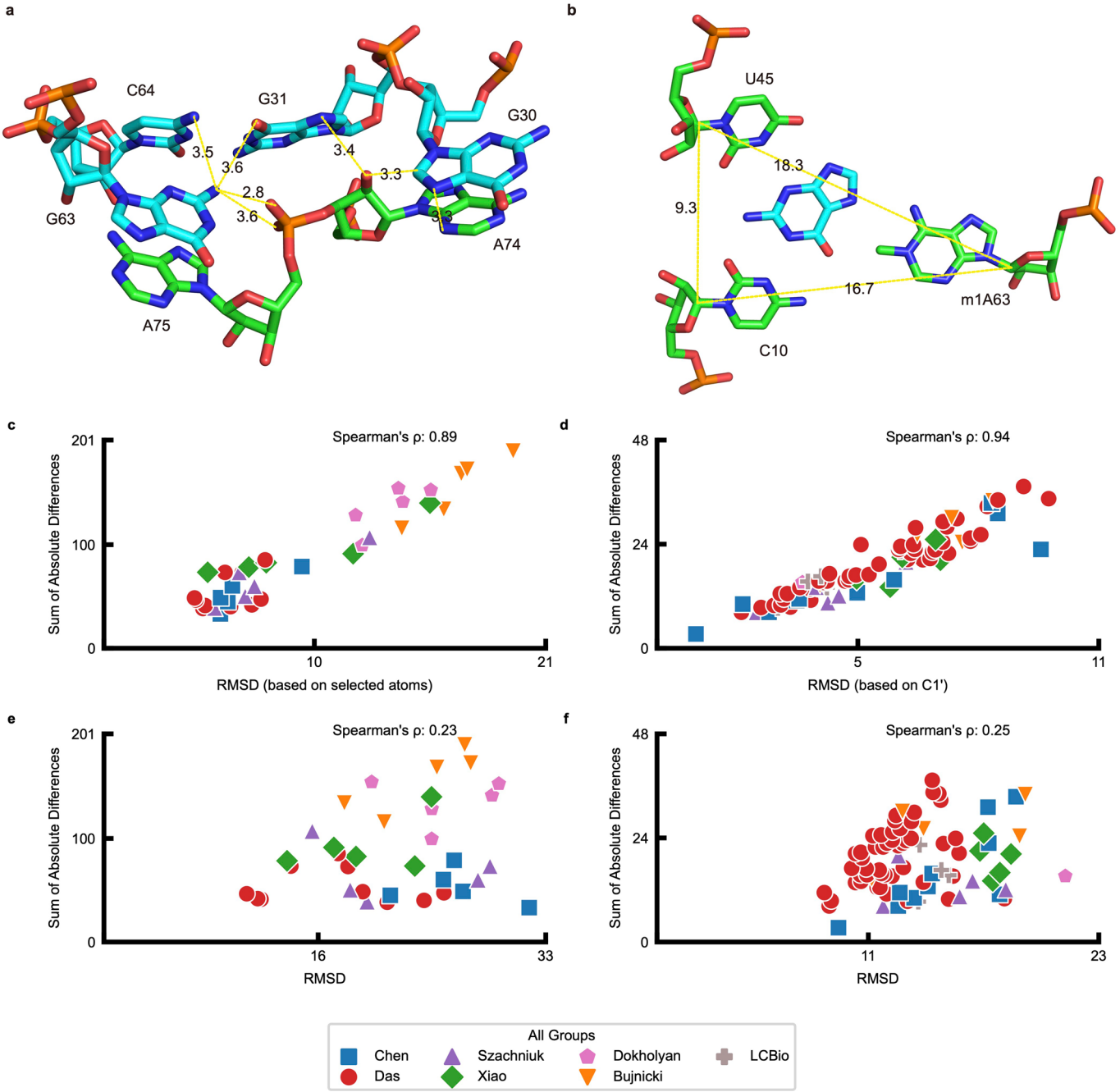

Extended Data Fig. 6 | Comparisons of core catalytic regions in PZ22 and PZ34 from the human group predictions in the Ribozyme category. (**a**) The structure shows key distances between selected atoms in the core catalytic regions of the experimental structure of PZ22. These selected atoms include G63-N2, C64-N4, G31-O6, A75-OP (minimum of A75-OP2 or A75-OP1), A74-O2′, G31-N7, G30-C8, A74-N3, and G30-N7. (**b**) The structure shows distances between selected atoms in the core ligand-binding region of the experimental structure of PZ34. The selected atoms include U45-C1′, A63-C1′, and C10-C1′. (**c**) The dot plot shows the correlation between the sum of distance differences (predicted vs. crystal model) of the selected atoms (as shown in panel a) in PZ22 and the r.m.s.d. of selected atoms of the selected nucleotides (G63, C64, G31, A75, A74, G30) (P = 0.00). (**d**) The dot plot shows the correlation between the sum of distance differences of C1′ atoms (predicted vs. crystal model) in PZ34 and the r.m.s.d. of C1′ atoms of the selected nucleotides (U45, A63, C10) (P = 0.00). (**e**) The dot plot shows the correlation between the sum of distance differences of the selected atoms (predicted vs. crystal model) in PZ22 and the global r.m.s.d. (P = 0.19). (**f**) The dot plot shows the correlation between the sum of distance differences of C1′ atoms (predicted vs. crystal model) in PZ34 and the global r.m.s.d. (P = 0.02).

https://doi.org/10.1038/s41592-024-02543-9

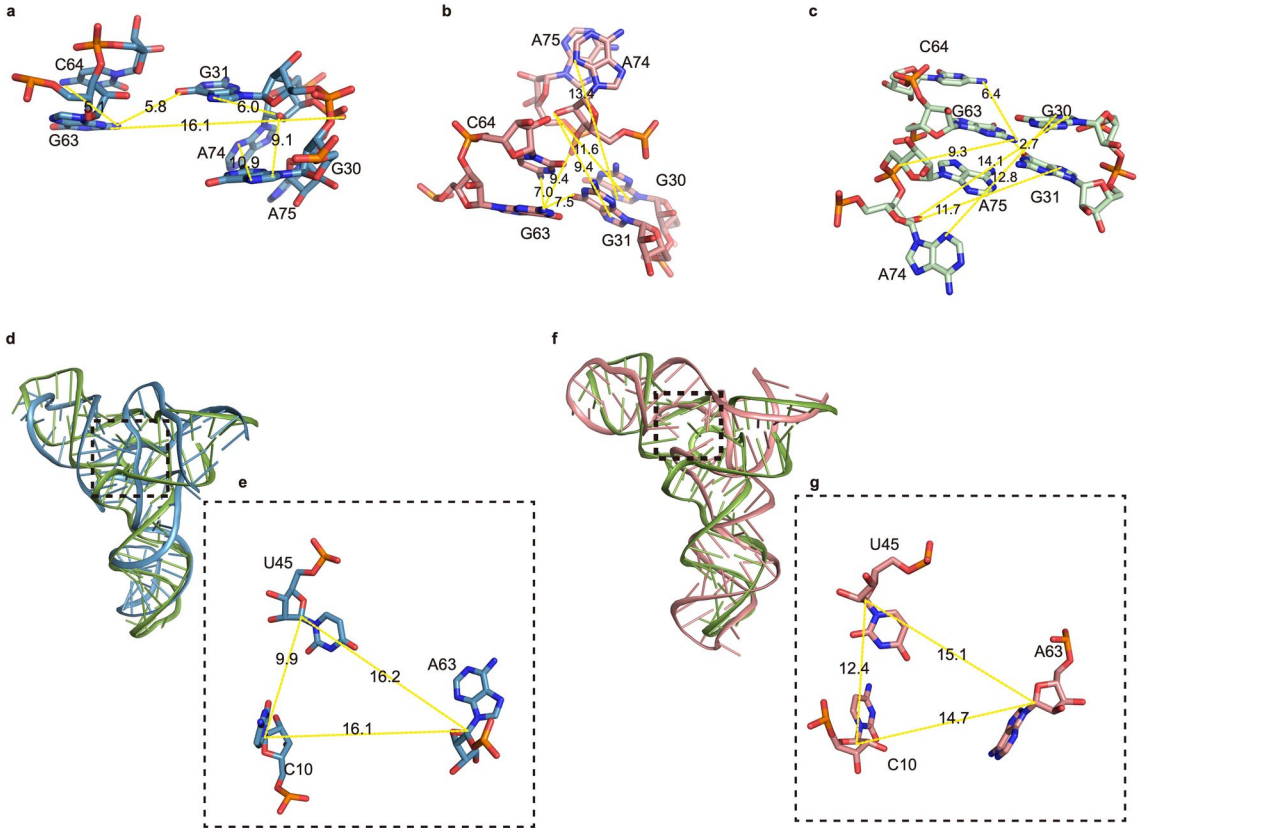

Extended Data Fig. 7 | Comparisons of the Core Catalytic Regions between the experimental and predicted structures for PZ22 and PZ34 (Human Group Predictions). (**a**–**c**) For PZ22, the panels illustrate selected key interatomic distances (G63-N2, C64-N4, G31-O6, A75-OP (the minimum value of A75-OP2 or A75-OP1), A74-O2′, G31-N7, G30-C8, A74-N3, and G30-N7) within the core catalytic regions predicted by Chen (model: Chen_3, r.m.s.d.: 31.8 Å), Das (model: Das_7, r.m.s.d.: 21.2 Å), and Szachniuk (model: Adamiak_2; r.m.s.d.:19.7 Å) groups. The environment in the experimental structure is shown in Extended Data Fig. 6a. Notice that in the experimental structure (Extended Data Fig. 6a), A74 is close to G30 and A75 to G63. In none of the models, this pattern is respected; they all show A74 and A75 stacked or in close proximity. (**d**) For PZ34, the panel shows the global overlay between the target (in green) and Chen model (in blue, model: Chen_3) (global r.m.s.d.: 9.4 Å). (**e**) The panel shows selected interatomic distances (U45-C1′, A63-C1′, and C10-C1′) in the core catalytic region of Chen model (model: Chen_3). (**f**) The panel displays the global overlay between the target (in green) and Das model (in red, model: Das_2) (global r.m.s.d.: 9.0 Å). (**g**) The panel highlights the interatomic distances in the core catalytic region of Das model (model: Das_2), focusing on selected atoms U45-C1′, A63-C1′, and C10-C1′. The environment in the experimental structure is shown in Extended Data Fig. 6b.

https://doi.org/10.1038/s41592-024-02543-9

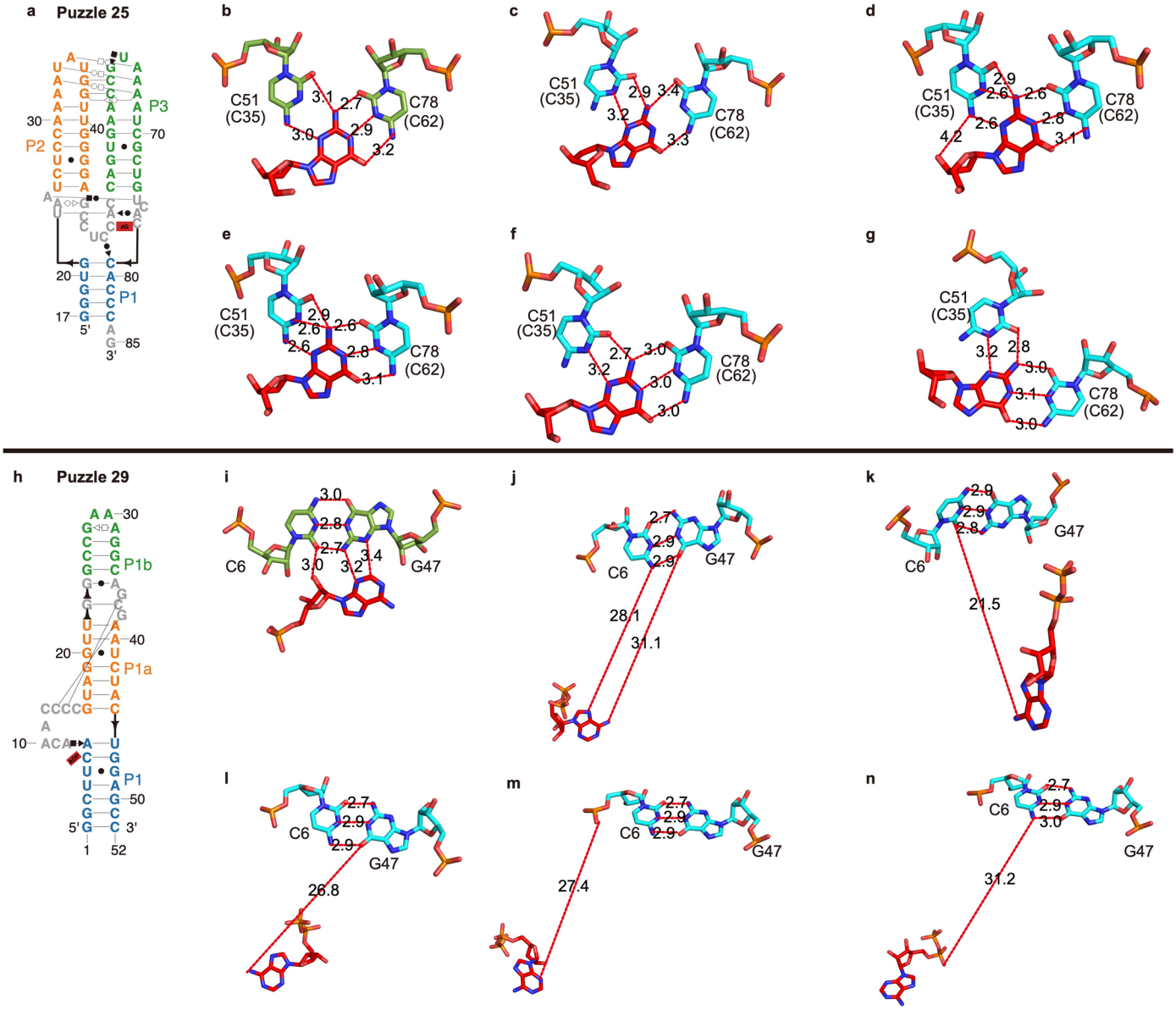

Extended Data Fig. 8 | Detailed analysis of the ligand-binding sites in Puzzle 25 and Puzzle 29 in the Riboswitch category. (**a**) Diagram showing the contacts in the crystal structure (PDB ID:6p2h) corresponding to PZ25. The ligand, 2′-deoxyguanosine (dG), is shown in a red rectangle. (**b**) The recognition mode of the ligand (in red and blue) in the crystal structure. (**c**) The recognition mode of the ligand in the best-predicted model (Chen_5, r.m.s.d. = 2.55 Å). (**d**) The recognition mode of the ligand in the next best-predicted model (Adamiak_1, r.m.s.d. = 2.68 Å). (**e**) The recognition mode of the ligand in the following predicted model (Adamiak_3, r.m.s.d. = 2.69 Å). (**f**) The recognition mode of the ligand in the following predicted model (Chen_8, r.m.s.d. = 2.71 Å). (**g**) The recognition mode of the ligand in the following predicted model (Chen_3, r.m.s.d. = 2.84 Å). (**h**) Diagram showing the contacts in the crystal structure (PDB ID:6tb7) corresponding to PZ29. The ligand, ADP, is shown in a red rectangle. The r.m.s.d. between 6tb7 (ligand AMP) and 6tf1 (ligand ADP) is 0.2 Å; thus either one can be used for comparisons. The numbers inside the parentheses are the numbers of the bases in the predicted structure. (**i**) The recognition mode of the ligand (in red and blue) in the crystal structure. (**j**) The recognition mode of the ligand in the best-predicted model (RNAComposer_1, r.m.s.d. = 4.30 Å). (**k**) The recognition mode of the ligand in the next best-predicted model (Chen_9, r.m.s.d. = 4.68 Å). (**l**) The recognition mode of the ligand in the next best-predicted model (Szachniuk_3, r.m.s.d. = 4.79 Å). (**m**) The recognition mode of the ligand in the following predicted model (RNAComposer_5, r.m.s.d. = 4.81 Å). (**n**) The recognition mode of the ligand in the following predicted model (RNAComposer_3, r.m.s.d. = 4.83 Å).

https://doi.org/10.1038/s41592-024-02543-9

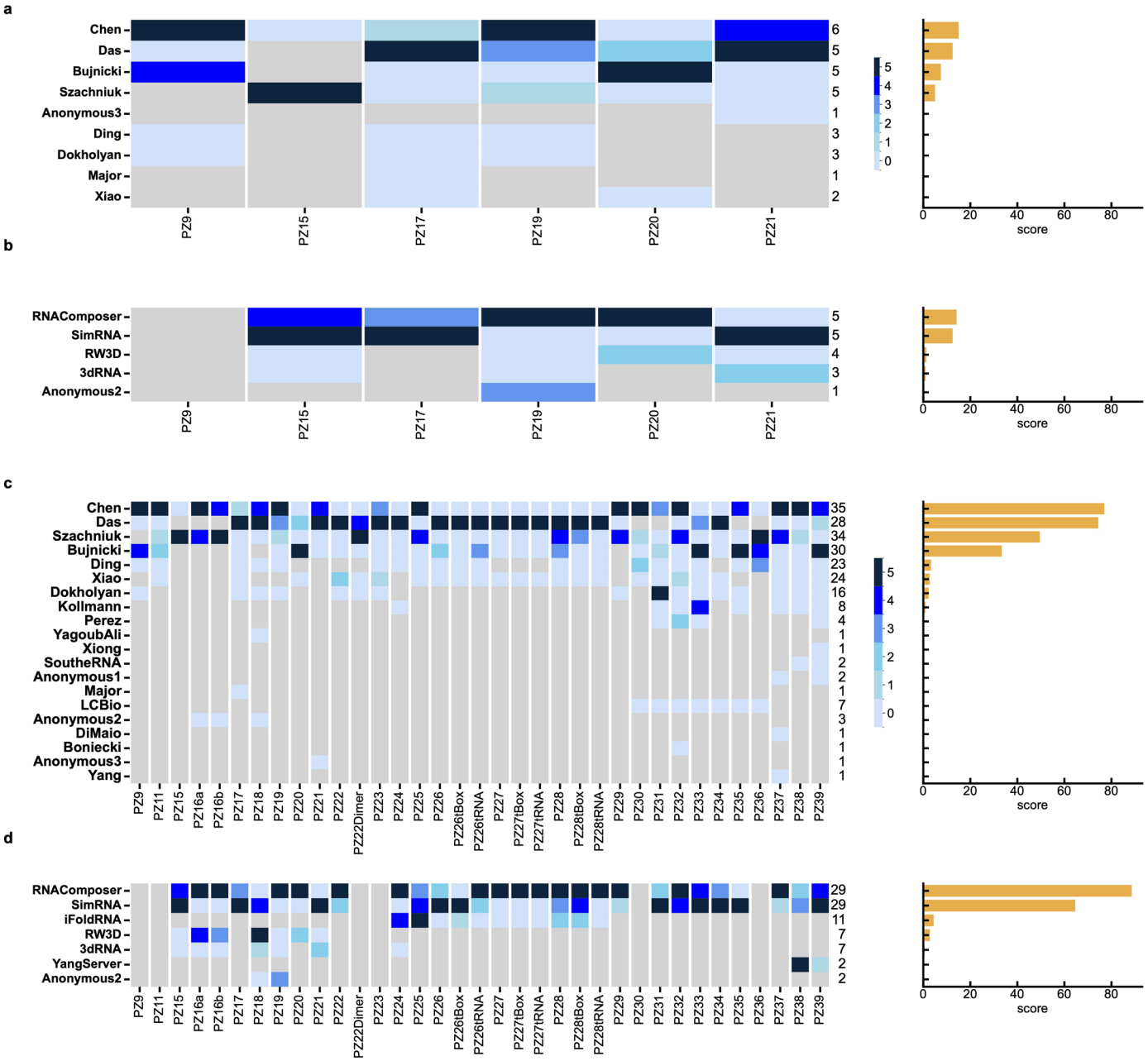

Extended Data Fig. 9 | Comparisons between the rankings of the human and web-based predictions in RNA Puzzles Round IV[4] and Round V (this paper). Rankings from Puzzles Round IV[4] are shown for human predictions in (**a**) and web-based predictions in (**b**). Rankings from the cumulated Puzzles Round IV and V, are shown for human predictions in (**c**) and web-based predictions in (**d**). The color scheme ranges from dark blue (5, best r.m.s.d.) to light gray (0, no models in the top five or no submissions). When a single group has submitted models for a Puzzle, the results are not counted. The right columns show the total number of valid RNA puzzles each group submitted. The final score on the left is the ratio of the sum to the total number of Puzzles (Round IV: 6, Round IV and V: 35). For the Das group, the models obtained by different methods are grouped together (see Supplementary Table 5). The web-based predictions include RNAComposer from the Szachniuk group (Polish Academy of Sciences), SimRNA from the Bujnicki group (International Institute of Molecular and Cell Biology in Warsaw), iFoldRNA from the Dokholyan group (Penn State College of Medicine, Hershey), RW3D from the Das group (Stanford University), YangServer from the Yang group (Shandong University), 3dRNA from the Xiao group (Huazhong University of Science and Technology), and LeeAS from the Lee group (Korea Institute for Advanced Study, Major from Francois Major (Université de Montréal)).

nature portfolio

Corresponding author(s): Zhichao Miao and Eric Westhof

Last updated by author(s): June 18,2024

Reporting Summary

Nature Portfolio wishes to improve the reproducibility of the work that we publish. This form provides structure for consistency and transparency in reporting. For further information on Nature Portfolio policies, see our Editorial Policies and the Editorial Policy Checklist.

Statistics

For all statistical analyses, confirm that the following items are present in the figure legend, table legend, main text, or Methods section.

n/a	Confirmed	
☐	☒	The exact sample size (*n*) for each experimental group/condition, given as a discrete number and unit of measurement
☐	☒	A statement on whether measurements were taken from distinct samples or whether the same sample was measured repeatedly
☒	☐	The statistical test(s) used AND whether they are one- or two-sided *Only common tests should be described solely by name; describe more complex techniques in the Methods section.*
☒	☐	A description of all covariates tested
☒	☐	A description of any assumptions or corrections, such as tests of normality and adjustment for multiple comparisons
☒	☐	A full description of the statistical parameters including central tendency (e.g. means) or other basic estimates (e.g. regression coefficient) AND variation (e.g. standard deviation) or associated estimates of uncertainty (e.g. confidence intervals)
☒	☐	For null hypothesis testing, the test statistic (e.g. *F*, *t*, *r*) with confidence intervals, effect sizes, degrees of freedom and *P* value noted *Give P values as exact values whenever suitable.*
☒	☐	For Bayesian analysis, information on the choice of priors and Markov chain Monte Carlo settings
☒	☐	For hierarchical and complex designs, identification of the appropriate level for tests and full reporting of outcomes
☒	☐	Estimates of effect sizes (e.g. Cohen's *d*, Pearson's *r*), indicating how they were calculated

Our web collection on statistics for biologists contains articles on many of the points above.

Software and code

Policy information about availability of computer code

Data collection	All the prediction results and codes used are publicly available at www.rnapuzzles.org.
Data analysis	The evaluation tools are described and available in the RNA-Puzzles Toolkit(https://github.com/RNA-Puzzles/RNA-Puzzles-toolkit-overview). Software versions used: biopython (1.78) rna-tools (3.20) MC-Annotate (1.5, using mccore 1.6.2 i686 pc linux-gnu) e3nn (https://doi.org/10.5281/zenodo.5090150) ARES (https://zenodo.org/records/6893040) Deformation Profile (1.0.1) OpenStructure(2.8) or Singularity containers (https://git.scicore.unibas.ch/schwede/openstructure/tree/2.8.0/singularity) MolProbity (http://molprobity.biochem.duke.edu/index.php?MolProbSID=d7352nhhc5n7or1i77eldkkjj5&eventID=16) RNA-align (20190201) For the codes associated with the reproducibility of all figures, readers are encouraged to refer to the following URL: https://github.com/RNA-Puzzles/PuzzlesRoundV-reproducibility, software versions used: Python (3.10.6) pandas (1.5.2) matplotlib (3.6.2) seaborn (0.11.2) numpy (1.23.3) dos2unix (7.4.2)

scipy (1.10.0)

For manuscripts utilizing custom algorithms or software that are central to the research but not yet described in published literature, software must be made available to editors and reviewers. We strongly encourage code deposition in a community repository (e.g. GitHub). See the Nature Portfolio guidelines for submitting code & software for further information.

Data

Policy information about availability of data

All manuscripts must include a data availability statement. This statement should provide the following information, where applicable:

- Accession codes, unique identifiers, or web links for publicly available datasets
- A description of any restrictions on data availability
- For clinical datasets or third party data, please ensure that the statement adheres to our policy

All data for computational validation were collected from RCSB PDB (https://www.rcsb.org/) and RNA-Puzzles (https://www.rnapuzzles.org/):
PDB ID (Corresponding Puzzle)
5lys (PZ11), 6y0y (PZ16a), 6y0t (PZ16b),5tpy (PZ18),6jq5 (PZ22 and P22dimer),6e8u (PZ23), 6ol3 (PZ24),6p2h (PZ25),6pmo (PZ26/26T-box), 6pom (PZ27/27T-box), 6ufm (PZ28/28T-box), 6tb7 (PZ29), 7bg9(PZ30), 7mlx (PZ31),7eoj (PZ32),7elp/7elq/7elr/7els(PZ33),7v9e (PZ34),7qr4 (PZ35), 7qr3 (PZ36), 8gxc (PZ37), 8hb8 (PZ38),8dp3 (PZ39).

Human research participants

Policy information about studies involving human research participants and Sex and Gender in Research.

Reporting on sex and gender	The study does not involve any experiments, and all calculations are deterministic and can be reproducible.
Population characteristics	The study does not involve any experiments, and all calculations are deterministic and can be reproducible.
Recruitment	The study does not involve any experiments, and all calculations are deterministic and can be reproducible.
Ethics oversight	The study does not involve any experiments, and all calculations are deterministic and can be reproducible.

Note that full information on the approval of the study protocol must also be provided in the manuscript.

Field-specific reporting

Please select the one below that is the best fit for your research. If you are not sure, read the appropriate sections before making your selection.

☒ Life sciences ☐ Behavioural & social sciences ☐ Ecological, evolutionary & environmental sciences

For a reference copy of the document with all sections, see nature.com/documents/nr-reporting-summary-flat.pdf

Life sciences study design

All studies must disclose on these points even when the disclosure is negative.

Sample size	Not applicable
Data exclusions	Not applicable
Replication	Not applicable
Randomization	Not applicable
Blinding	Not applicable

Reporting for specific materials, systems and methods

We require information from authors about some types of materials, experimental systems and methods used in many studies. Here, indicate whether each material, system or method listed is relevant to your study. If you are not sure if a list item applies to your research, read the appropriate section before selecting a response.

Materials & experimental systems

n/a	Involved in the study
☒	☐ Antibodies
☒	☐ Eukaryotic cell lines
☒	☐ Palaeontology and archaeology
☒	☐ Animals and other organisms
☒	☐ Clinical data
☒	☐ Dual use research of concern

Methods

n/a	Involved in the study
☒	☐ ChIP-seq
☒	☐ Flow cytometry
☒	☐ MRI-based neuroimaging